JGR Solid Earth

RESEARCH ARTICLE
10.1029/2019JB017970

A Joint Inversion for Three-dimensional *P* and *S* Wave Velocity Structure and Earthquake Locations Beneath Axial Seamount

Christian Baillard[1], William S.D. Wilcock[1], Adrien F. Arnulf[2], Maya Tolstoy[3], and Felix Waldhauser[3]

[1]School of Oceanography, University of Washington, Seattle, WA, USA, [2]Institute for Geophysics, University of Texas, Austin, TX, USA, [3]Lamont-Doherty Earth Observatory, University of Columbia, Palisades, NY, USA

Key Points:
- An inversion for hypocenters and velocity on Axial Seamount images low V_P and V_S in the caldera indicative of altered and fractured rock
- Low V_P/V_S beneath the hydrothermal vent fields in the southern caldera is consistent with the presence of hydrothermal vapor
- The 3-D velocity models yield hypocenters that resolve an inward-dipping ring fault inside the network connecting to the east caldera wall

Supporting Information:
- Supporting Information S1

Correspondence to:
W. S. D. Wilcock,
wilcock@uw.edu

Citation:
Baillard, C., Wilcock, W. S. D., Arnulf, A. F., Tolstoy, M., & Waldhauser, F. (2019). A joint inversion for three-dimensional *P* and *S* wave velocity structure and earthquake locations beneath axial seamount. *Journal of Geophysical Research: Solid Earth*, *124*, 12,997–13,020. https://doi.org/10.1029/2019JB017970

Received 3 MAY 2019
Accepted 16 NOV 2019
Accepted article online 21 NOV 2019
Published online 12 DEC 2019

Abstract Axial Seamount is a prominent volcano located at the intersection of the Juan de Fuca Ridge and the Cobb-Eickelberg hot spot in the northeast Pacific Ocean that has erupted in 1998, 2011, and 2015. The 2015 eruption was recorded by a seven-station seismic network in the southern part of the summit caldera that forms part of the Ocean Observatories Initiative Cabled Array. We utilize a data set of ~3,900 well-recorded earthquakes from January 2015 to February 2017 and a three-dimensional *P* wave velocity model obtained previously from active source data to conduct a joint inversion for three-dimensional *P* and *S* wave velocities and hypocentral parameters. The resulting velocity models are used to relocate >76,000 earthquakes with ≥10 arrival times. The velocity models reveal a low-velocity anomaly in the center of the southern caldera at depths less than ~2 km, which corresponds to the top of the magma chamber and is interpreted as a region that is intensely fractured by the cyclical deformation of the caldera. High velocities around the caldera rim are likely due to consolidated undeformed lava flows. Low V_P/V_S in the southern caldera is consistent with the presence of hydrothermal vapor. Low *S* wave velocities and high V_P/V_S in the northern caldera may indicate a region dominated by thin cracks caused by dike injection. The relocated earthquakes delineate outward-dipping ring faults more clearly than previous studies and image a subvertical inward-dipping fault within the network that connects to the east caldera wall and eruptive fissures.

Plain Language Summary Axial Seamount is a volcano in the northeast Pacific Ocean that has erupted in 1998, 2011, and 2015. The 2015 eruption was recorded by a small seismic network that is part of a cabled observatory that connects scientific instruments on the volcano to shore. We analyzed the recordings of 3,900 small earthquakes to determine how the speed of compressional and shear seismic waves varies spatially within the volcano. We use the results to locate 76,000 earthquakes that occurred under the volcano over 2 years. The speed of seismic waves is low beneath the southern part of the caldera. This region is heavily fractured because the volcano repeatedly inflates and deflates as magma enters the magma chamber and then erupts. The relative speed of seismic compressional and shear waves beneath the southern caldera is consistent with the presence of boiling water in the subsurface beneath several sites of hydrothermal venting on the seafloor. The earthquakes are mostly located on a buried fault that wraps all around the caldera and slopes outwards with some others located on a near vertical fault that forms the caldera wall.

1. Introduction

Mid-ocean ridges (MORs) extend 60,000 km across the seafloor and are the locus of creation of the oceanic crust that covers two-thirds of the Earth's surface and accounts for about 75% of the Earth's volcanism (Crisp, 1984; German et al., 2004). MORs are of interest to scientists not only because of their importance to plate tectonics but also because they are settings where geological, hydrothermal, biological, and oceanographic processes interact. Active and passive seismic experiments play a prominent role in understanding MORs because images of subsurface seismic properties can be used to infer geological structure, porosity and crack distributions, and regions of elevated temperature and partial melt, and earthquakes are sensitive to the stress distributions and deformation.

Over the past few decades, the structure of MORs has been constrained by active source reflection and refraction studies, based primarily on *P* wave recordings. A low-velocity upper layer, termed Layer 2A, is

interpreted as a layer of high porosity although there is some controversy as to whether the reflective low-velocity gradient at its base marks a transition to the sheeted dike layer or an alteration front (Christeson et al., 2007). The thickness of Layer 2A varies along axis from a few hundred meters to nearly a kilometer (Christeson et al., 2010) and is believed to be controlled by the pressure in the magma chamber rather than magma supply (Buck et al., 1997; Carbotte et al., 1998). Furthermore, Layer 2A thickness on fast and intermediate spreading ridges increases with distance from the ridge axis (Harding et al., 1993). This is believed to be because younger lava buries the initially shallow top of the sheeted dike complex. Below Layer 2A, velocities in the upper crust (Layer 2B) increase progressively with depth because of the effects of crack closure (e.g., Carlson, 2014; Spudich & Orcutt, 1980). Within the lower crust gabbros (Layer 3), velocity gradients are low and influenced primarily by composition (Sinton & Detrick, 1992).

Multichannel reflection studies show that a steady-state lens-shaped axial magma chamber is present at midcrustal depths along faster spreading MORs (Carbotte et al., 2006; Detrick et al., 1987, 1993) and that its depth tends to decrease with increased spreading rate and increased magma supply (Chen & Lin, 2004; Chen & Morgan, 1996). Reflection data have been widely used to infer along axis variations in the presence and properties of the axial magma chamber (e.g., Canales et al., 2006; Combier et al., 2015; Singh et al., 1998; Xu et al., 2014). Tomographic studies on the East Pacific Rise (Dunn et al., 2000) and Juan de Fuca Ridge (JdFR; Arnoux et al., 2019) show that the axial magma chamber is underlain in the lower crust by a steep-sided region of elevated temperatures and partial melt that broadens in the mantle. Reflection and tomographic imaging play a key role in studies to understand the nature and origins of along axis volcanic and tectonic segmentation of MORs (e.g., Arnoux et al., 2019; Carbotte et al., 2006, 2013; Magde et al., 2000; Toomey et al., 2007).

Microearthquake studies on MORs complement seismic imaging. They provide a direct means to observe tectonic deformation (Parnell-Turner et al., 2017; Toomey et al., 1985; Wilcock et al., 2002). For hydrothermal systems, they have been used to determine the patterns of hydrothermal cooling (Crawford et al., 2013; Golden et al., 2003; Sohn et al., 1999; Tolstoy et al., 2008), and microearthquakes are also an indicator of reaction driven fracturing (Pontbriand & Sohn, 2014) and hydrofracturing (Gudmundsson et al., 2002). For magmatic systems, microearthquakes are linked to magma chamber inflation (Levy et al., 2018; Wilcock et al., 2009; Wilcock et al., 2016) and local seismic networks complement hydroacoustic monitoring (Dziak et al., 2012) to observe diking-eruptive events (Tan et al., 2016; Tolstoy et al., 2006; Wilcock et al., 2016).

The earthquake locations for most MOR microearthquake studies are derived using 1-D velocity models. While the relative locations of nearby earthquakes can be constrained using techniques such as the double-difference method (Waldhauser & Ellsworth, 2000), absolute locations are likely to have considerable biases because the velocity structure of MORs is strongly heterogeneous. Improved earthquake locations would enhance interpretations that depend upon linking earthquake distributions to magmatic and tectonic features. At some MOR sites, 3-D active-source tomographic images of *P* wave velocities (V_P) are available to locate earthquakes (e.g., Sohn et al., 1998), but accurate earthquake locations also require good knowledge of *S* wave velocities (V_S; Gomberg, 1990). In addition, knowledge of the *S* wave structure contributes to structural interpretations because *Vs* has different sensitivities than V_P to properties of geological interest. In particular, for the upper crust, V_S is important for understanding crack distributions. High V_P/V_S ratios can indicate either a high porosity of fluid filled, connected pores, as would be the case for breccia, talus, and rubble (Hyndman, 1979) or the presence of thin (small aspect ratio) cracks that decrease V_S proportionately more than V_P (Kim et al., 2018; Sanders et al., 1995; Shearer, 1988).

At MORs, models of V_S are harder to obtain from refraction studies than V_P models because, with the exception a few studies that have used a source on the seafloor (e.g., Christeson et al., 1994), they are dependent upon the generation of coherent *P* to *S* converted phases at the seafloor or Layer 2A boundary. These must be picked as secondary phases on horizontal seismometer channels that are often noisier and less well coupled than the vertical seismometer and hydrophones channels used to pick *P* waves. Refraction data have been used to infer 1-D models of V_S structure on the Mid-Atlantic Ridge (MAR; Fowler, 1976) and East Pacific Rise (Bratt & Solomon, 1984; Vera et al., 1990), but only one 3-D tomographic V_S model has been obtained on an MOR (Kim et al., 2018). Kim et al. (2018) show that V_P/V_S in the sheeted dike layer in the Endeavour

Segment of the JdFR increases off-axis and interpret this in terms of the existence of thick cracks on-axis that promote hydrothermal circulation and focus vent fields at the seafloor.

An alternative approach is to invert earthquake arrival time data to simultaneously constrain the 3-D velocity structure and hypocenters. Such joint inversions are challenging because of the trade-off between hypocenters and velocity structure (e.g., Pavlis & Booker, 1980), but they are commonly used to study volcanoes on land (Lees, 2007). Some studies utilize only *P* wave arrivals to solve only for V_P and hypocenters (e.g., Molina et al., 2005; Prôno et al., 2009), but there are numerous examples of successful inversions using both *P* and *S* wave arrival data. For example, at Toba volcano, Northern Sumatra (Koulakov et al., 2009), and Krakatau volcano, Indonesia (Jaxybulatov et al., 2011), low V_P and V_S anomalies with high V_P/V_S ratios have been used to infer the presence of multiple levels of magma chambers in the crust at 5 km depth and down to a depth of 12 km. At Kluchevskoy volcanoes, Kamchatka, an inferred region of partial melt with high V_P/V_S near the base of the crust, is overlaid by intense seismicity that is interpreted in terms of high stresses due to magma ascent, water release, and phase transitions (Koulakov et al., 2011). At Redoubt volcano, Alaska (Benz et al., 1996) and Toba volcano (Koulakov et al., 2009), pipe-shaped structures with relatively low velocities and intense seismic activity, are observed above the magma chambers and are interpreted in terms of fluid migration in magmatic conduits. At Yellowstone, a region of low V_P and low V_P/V_S overlying an earthquake swarm is interpreted as a gas-filled region being fed from below by migrating fluids (Husen et al., 2004).

On MORs, joint inversions for earthquake locations and velocity structure are less common. Microearthquake data sets on the MAR have been inverted for 2-D V_P models (Kong, 1990; Toomey et al., 1988). At 23°N on the MAR, earthquake locations are consistent with normal faults subparallel to the Axial valley, and V_P beneath the central valley is lower by several percent, consistent with the presence of fractured material resulting from recent local magmatic injection and rapid hydrothermal quenching (Toomey et al., 1988). There have been only two joint inversions that solved for both V_P and V_S (Barclay et al., 2001; Barclay & Wilcock, 2004) and both only solved for 1-D structure. At 35°N on the MAR, Barclay et al. (2001) observed a decrease of V_P/V_S with depth and interpreted this in terms of a decreasing contribution from thin cracks to porosity. On the Endeavour segment of the JdFR, an inversion of a small number of explosive shots and microearthquakes that were mostly located at mid-crustal depths showed a poorly resolved trade-off between the vertical V_P and V_S structure and changes in average earthquake depth (Barclay & Wilcock, 2004).

In this paper, we use *P* and *S* wave arrival times from ~3,900 well-recorded earthquakes from the Ocean Observatories Initiative Cabled Array (OOI-CA; Wilcock et al., 2016) and a starting 3-D V_P model derived from active source *P* wave first-arrivals (Arnulf et al., 2018) to obtain 3-D V_P and V_S models beneath the caldera of Axial Seamount. This is the first 3-D crustal V_S model obtained by passive tomography on a MOR. We use the resulting 3-D velocity models to relocate a catalog of >76,000 earthquakes with a minimum of 10 arrival times using a nonlinear location algorithm. We interpret these results in terms of the structure of the caldera, the impacts of deformation due to the 2015 eruption, and the effect of hydrothermal processes.

2. Geological Background

Axial seamount is an active volcano in the northeast Pacific Ocean located at the intersection of two magmatic systems, the JdFR oceanic spreading center and the Cobb-Eickelberg hotspot (130.00°W, 45.95°E, Figure 1). It is the most prominent volcano on the JdFR with a summit that rises ~1000 m above the seafloor to 1400 m below sea level. The summit is characterized by a horseshoe-shaped caldera measuring 9 km by 3 km that is elongated in the N-S direction and open at its southern end. Three high temperature hydrothermal vent fields are located within the caldera, CASM at the north end, ASHES at the southwestern caldera wall, and international district (ID) at the south end, and there are several sites of diffuse venting near the southeastern caldera wall (Figure 1).

Axial Seamount has been intensively studied for over 30 years (Hammond et al., 2015; Johnson & Embley, 1990; Wilcock et al., 2018), during which time three eruptions have been observed in 1998, 2011, and 2015 (Caress et al., 2012; Chadwick et al., 2012, 2016; Dziak et al., 2012; Dziak & Fox, 1999; Fox, 1999; Nooner

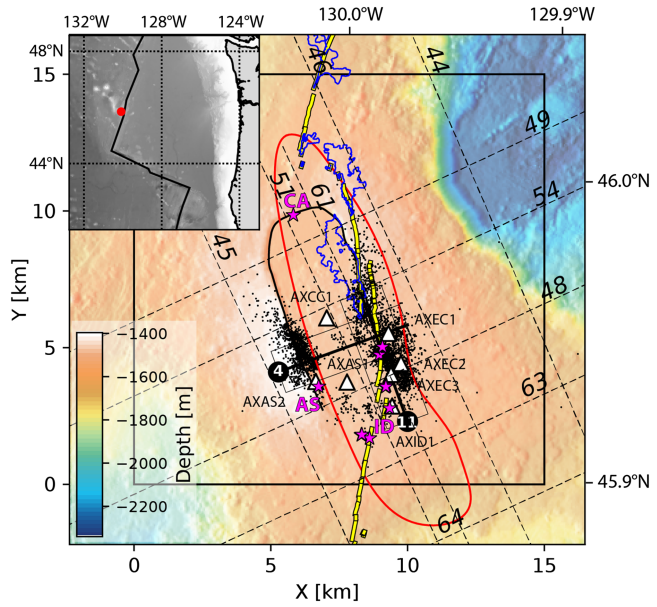

Figure 1. Bathymetric map showing the location of the 3,894 earthquakes (dots) selected for tomographic inversion. Locations are obtained using LOTOS and the 1-D V_P and V_S models used by Wilcock et al. (2016). The main active vent fields are shown as labelled pink stars (CA: CASM; AS: ASHES; ID: International District) and diffuse vents as unlabeled stars. The seven ocean bottom seismometers are shown as white triangles that are labeled with the station name (two symbols are partially obscured by the ASHES and International District vent fields). The outline of the axial magma chamber is shown by a red line (Arnulf et al., 2014, 2018). The lava flows for the 2015 eruption are shown by blue lines and the fissures for the 2011 and 2015 eruptions by yellow lines (Chadwick et al., 2016). The black square shows the area of the velocity models for our inversions, which has origin at 130.1°W/45.9°N and depth of 1.525 km below sea surface. Labelled black lines show the locations of cross-sections 4 and 11 in Figure 2.

& Chadwick, 2016; Wilcock et al., 2018; Wilcock et al., 2016). Since late 2014, Axial seamount has been continuously monitored with the deployment of the OOI-CA, a wired-to-shore real time regional observatory that includes oceanographic, geophysical, and hydrothermal instruments (Kelley et al., 2014). At the summit of Axial seamount, the OOI-CA spans the southern half of the caldera and supports a network of five short-period and two broadband three component seismometers sampling at 200 Hz (station names and locations are shown Figure 1), geodetic sensors to measure bottom pressure and tilt, and hydrothermal sensors in the ASHES and ID vent fields.

The OOI-CA network provided a remarkable opportunity to monitor the 24 April 2015 eruption. Prior to the eruption, the caldera inflated at a near constant rate of 61 cm/year (Nooner & Chadwick, 2016), which was accompanied by intense and increasing seismic activity, with the rate of earthquakes reaching ~2,000 per day a month before the eruption (Wilcock et al., 2016). The distribution of earthquakes before, during, and after the eruption revealed an outward-dipping ring fault (dipping at 52°–70°) that partially accommodates the inflation and deflation of the magma chamber (Levy et al., 2018; Nooner & Chadwick, 2016; Wilcock et al., 2016). The majority of earthquakes occur under the eastern wall of the caldera with most of the remaining earthquakes occurred along the western wall. Levy et al. (2018) relocated 19,049 earthquakes using the hypoDD algorithm (Waldhauser & Ellsworth, 2000) and computed composite focal mechanisms from first motion polarities and S/P amplitude data using the HASH algorithm (Hardebeck et al., 2008). Focal mechanisms revealed a pattern of normal slip on the ring faults prior to the eruption and reverse slip during the eruption consistent vertical uplift and subsidence of the caldera floor along the outward-dipping faults.

The eruption was marked by 2.45 m of deflation and a 10-hr seismic "crisis" followed by a rapid drop in the rate of seismicity over several weeks to <10 per day. The network did not record earthquakes from the northward propagation of a dike, but impulsive acoustic signals located on the seafloor (Wilcock et al., 2016) recorded the position of numerous lava flows identified in the northern caldera and up to 15 km along the north rift (Figure 1; Clague et al., 2017).

The V_P structure under Axial Seamount has been studied by active-source experiments. West et al. (2001) inverted *P* wave arrival times for 5,025 airgun shots recorded on six ocean bottom seismometers (OBSs) to obtain the first 3-D V_P model under Axial Seamount. Their study revealed the presence of a large low-velocity magma chamber beneath the caldera at 2.5–3.5 km depth. Arnulf et al. (2014) analyzed four multichannel seismic (MCS) lines from an experiment that extended along the JdFR (Carbotte et al., 2008) and applied full waveform inversion to constrain a detailed 2-D V_P model beneath each line. They inferred that the magma chamber is 3-km-wide by 14-km-long, at a depth of 1.1 to 2.3 km, with a thickness of ~1 km and a volume of melt of 8–30 km^3. Arnulf et al. (2018) combined the OBS data of West et al. (2001) with data from 12 MCS profiles into a joint tomographic inversion to obtain a more detailed 3-D V_P model under Axial Seamount. In addition to the magma chamber beneath the caldera, they inferred the existence of a secondary magma reservoir east of the caldera.

Imaging the shallow structure between the seafloor and the magma chamber is challenging in deep-water environments due to the absence of turning rays at shallow depths. Arnulf et al. (2018) simulated a synthetic on bottom experiment (Arnulf et al., 2011; Harding et al., 2007) by artificially moving receivers and sources of the MCS data set onto the seafloor. The resulting data set reveals refraction rays turning just below the seafloor and appearing as first arrivals. Arnulf et al. (2014) imaged a network of upper crustal fractures interpreted as pathways for molten material from the magma reservoir to the surface. Arnulf et al. (2018) showed

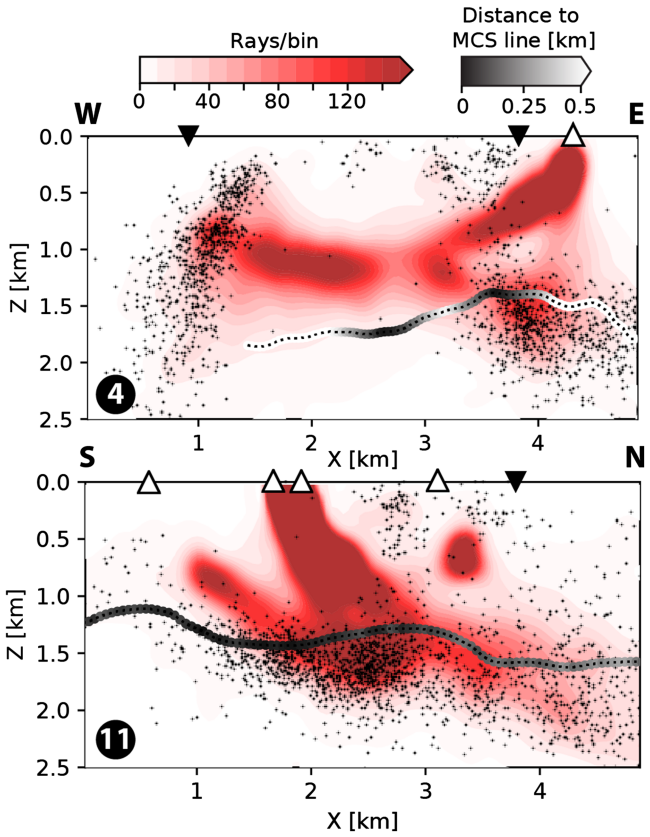

Figure 2. Orthogonal cross-sections along the profiles labelled 4 and 11 on Figure 1 showing the projected location of earthquakes (dots) used in the inversions and OBSs (white triangles) that are within 0.8 km of the profile (dots) and the density of rays per 0.1 km × 0.1 km × 0.1 km bin obtained from ray tracing with the LOTOS algorithm (red color scale). Profile numbers are chosen to be consistent between figures. The top of the axial magma chamber is plotted as a dotted line with a gray scale indicative of the distance to the nearest MCS lines (dashed lines on Figure 1) used to constrain the roof of the magma chamber in the 3-D V_P model (Arnulf et al., 2018; black: 0 km separation; white >0.5 km). Inverted black triangles are projections of the caldera walls.

a ring of high velocities surrounding the caldera. Velocities within this ring are on average 0.5 km/s higher than those within the caldera. The ring of high velocities corresponds to a relative thin Layer 2A (0.4 to 0.75 km) while the low-velocity central caldera corresponds to slightly thicker Layer 2A (0.75 to 0.90 km). The greater thickness of Layer 2A within the caldera suggests a subsiding caldera floor, acting as a trap for the ponding lava flows.

Arnulf et al. (2018) also relocated the seismicity recorded by the OOI-CA network by applying a grid search method to the arrival times of Wilcock et al. (2016) and Wilcock et al. (2017) assuming the 3-D V_P model and a simple transfer function relating V_P to V_S and calculating ray paths using a shortest-path method (Moser, 1991). The catalog suggests that the western and eastern outward-dipping fault dip at 42° and 60°, respectively, compared to dips of 52° and 70° inferred by (Wilcock et al., 2016) and 68° and 67° inferred by Levy et al. (2018). Beneath the northern part of the caldera and just to the north of the network, the relocated earthquakes define inward-dipping faults extending from the east and west caldera walls and dipping at 40°–47°. These faults were not observed in the other studies.

3. Data

3.1. Seismic Catalog

We use data from January 2015 to February 2017 from the near real-time automated earthquake catalog of Wilcock et al. (2018), Wilcock et al. (2016) and Wilcock et al. (2017). The catalog contains 107,130 events with 601,816 *P* wave picks and 584,150 *S* wave picks determined using a Kurtosis picking algorithm (Baillard et al., 2014). In this catalog, earthquakes were located using a linearized inverse method (HYPOINVERSE, Klein (2002)) and 1-D V_P and V_S models. The V_P model used to locate the earthquakes was obtained by averaging the structure of Arnulf et al. (2014, 2018) within and near the caldera to obtain a 40-layer 1-D velocity model, while the V_S structure was based on the assumptions that the depth-dependent variation of V_P/V_S is similar to that inferred from microearthquake data at the endeavor segment of the JdFR (Barclay & Wilcock, 2004; Wilcock et al., 2002).

In order to maximize the robustness of the joint inversion for hypocenters and velocity, we use a subset of the catalog that comprises the best-recorded earthquakes located within or near the network. To be selected, earthquakes must (1) have a root-mean squared travel time residual of <0.1 s, (2) have ≥5 *P* wave picks each with a weight ≥0.5 (*P* wave weights range from 0 to 1, weights are based on signal over noise ratios), (3) have ≥5 *S* wave picks each with a weight ≥0.2 (*S* wave weights range from 0 to 0.33), and (4) be located between 130.1°E and 129.9°E and between 45.9°N to 46.0°N. These criteria yield a data set of 3,894 earthquakes with 24,265 *P* picks (average weight of 0.92) and 20,065 *S* picks (average weight of 0.29; Figures 1 and 2). We assume an a priori picking error of 0.02 s for fully weighted arrivals with errors inversely proportional to the weight.

3.2. Starting 3-D V_P Model

We use the 3-D V_P model of Arnulf et al. (2018) as the starting model for our inversions. This 3-D V_P model covers a 40 km long by 30 km wide area centered on Axial Seamount and images the velocity structure to an estimated depth of ~4.5 km. It is discretized on a 100 m × 100 m × 50 m (X × Y × Z) grid. As most of the earthquakes of our subcatalog are located beneath the caldera, we extracted a smaller volume that is 15 × 15 × 4 km (X × Y × Z) and discretized uniformly at 0.1 km.

Table 1
LOTOS Parameters (Koulakov, 2009) Used in the Joint Inversion to Obtain the Final 3-D V_P and V_S Models

Parameter name	Preferred value	Description
max_bend	1 km	Maximum deviation from a straight ray.
min_segm	0.2 km	Minimum length of subdivided segments along the ray
num_LSQR	80	Number of iterations in the LSQR process
reg_p/reg_s	0/0	Regularization parameters. Limits the variations of *P*/*S* velocities through successive iterations. 0 means no regularization.
smooth_p/ smooth_s	0.3/0.4	Level of smoothing to be applied to the velocity models. Limits amplitude variations between neighboring cells. 0 means no smoothing.
w_vp/w_vs	1/1	Weights to be applied to the *P*/*S* velocity models. Equal weights insure that both models will have similar influence on the residuals. 0 means no weighting
w_sta_p/ w_sta_s	0.001/0.001	Weights to be applied to *P*/*S* station corrections. 0 means station correction will remain small.
w_hyp	5	Weight to be applied to hypocenter shifts.
w_time	1	Weight to be applied to origin time.

The starting 3-D V_P model used by Arnulf et al. (2018) was derived from both a 1-D V_P model for depth <1.2 km (Arnulf et al., 2014) and an earlier 3-D V_P model at larger depths (West et al., 2001). Arnulf et al. (2018) used MCS profiles to constrain the roof of the magma chamber in their inversion, so the magma chamber is constrained based on *a priori* information about the location of the magma chamber. To avoid possible biases in our inversion due to sharp velocity changes across the magma chamber roof, we removed the low-velocity magma chamber obtained by Arnulf et al. (2018) and interpolated the velocities from above using a 3-D nearest-neighbor algorithm. This has little effect on the location and ray computation as most earthquakes are located above the magma chamber.

4. Methods

4.1. Tomography

We use a modified version of the LOTOS nonlinear algorithm for passive seismic tomography (see Koulakov (2009) for details). LOTOS, in its original form, only allows the use of starting 1-D velocity profiles, but we modified it in order to use the 3-D V_P model of Arnulf et al. (2018) as the starting model. The algorithm performs a simultaneous inversion for V_P and V_S structure, earthquake locations, origin times, and station corrections. The 3-D ray tracing for the forward problem is based on a ray bending method (Um & Thurber, 1987), which utilizes Fermat's principle of time minimization, described in (Koulakov et al., 2009). The bending of the rays is controlled by two key parameters, the maximum displacement of the ray from a straight path (max_bend) and the minimum length of the subdivided segments along the ray (min_segm). Our choice of parameters (Table 1) allows significant ray bending to account for the large velocity heterogeneities expected in the region.

The partial derivative matrix in the joint inversion for velocity and hypocenter is complemented by two submatrices that affect the velocity perturbations, a regularization matrix and a smoothing matrix. The regularization matrix has a diagonal structure with only one element in each row. The corresponding elements in the data vector are zero. Increasing the weight (reg_p, reg_s) of this matrix reduces the amplitude of the inverted V_P and V_S anomalies. The smoothing matrix contains in each row two nonzero elements of equal magnitude and opposite sign that correspond to all combinations of neighboring nodes in the V_P and V_S models. The corresponding elements in the data vector are also zero. Increasing the weight (smooth_p, smooth_s) of this block reduces the difference between anomalies in neighboring nodes, hence smoothing the resulting V_P and V_S models. Multiple checkerboard tests (see section 4.2) were applied to determine and fine-tune these parameters (Table 1).

Weights for the velocity models (w_vp, w_vs) are required, and we used equal weights for both models. Weights for hypocentral shift (w_hyp) and origin time (w_time) provide a mean to control the relative perturbations to hypocentral parameter and velocity and were defined based on Koulakov (2009). LOTOS also allows for station correction (w_sta_p, w_sta_s) but because we wanted to map travel time variations into velocity, we gave these a very small weight (Table 1). The inversion is performed using an LSQR method

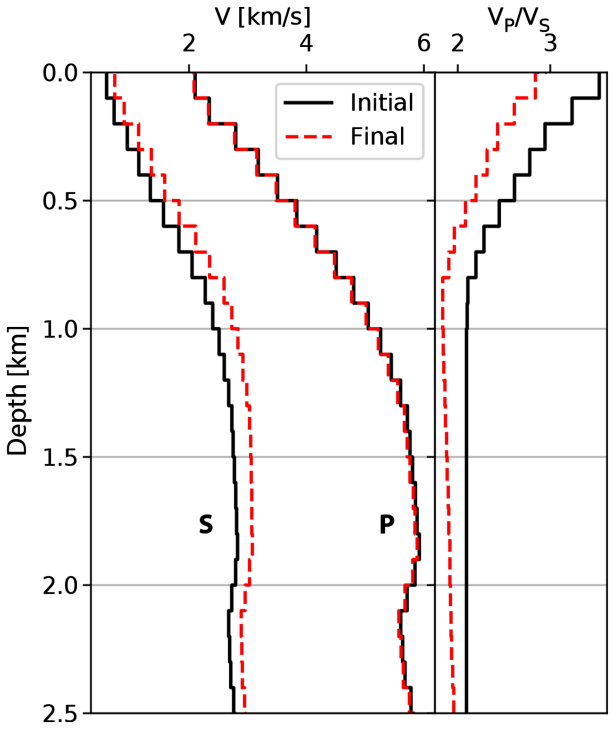

Figure 3. Starting (black) and final (dashed red) mean 1-D velocity profiles. Except for the starting V_S model, which is one-dimensional, these profiles were obtained by averaging the 3-D models at each depth inside the region delimited by the circle drawn on Figure 7a. The starting 1-D V_P/V_S profile was chosen after performing multiple 1-D tests and comparing the locations and the time residuals (Figure S1 shows all 17 profiles tested).

(Paige & Saunders, 1982; Sluis & Vorst, 1987). To ensure convergence of the LSQR process, we chose a relatively high value for the maximum number of iterations (num_LSQR; Table 1).

LOTOS cannot incorporate the individual weights that were assigned to P and S phases based on signal to noise ratio in the automated catalog (Wilcock et al., 2016). This is a reason why we chose to invert a subset of the catalog that comprised the best recorded earthquakes with good quality picks. For each earthquake at each station, when no S pick exists, the P pick residual is assigned a weight of 1. When no P pick exists, the S pick residual is assigned a weight of 0.6 to reflect the larger uncertainty of S picks. When P and S picks both exist for a station, their differential residuals are assigned a weight of 1. Assigning the same weight for the P residuals and *S-P* residuals ensures good coherency between the V_P and the V_S models (Koulakov, 2009).

The inversion requires a reasonable starting model for both V_P and V_S. The starting three-dimensional V_P of Arnulf et al. (2018) is well constrained by active source data, but there are few constraints on V_S. We explored three different approaches to obtain a suitable starting V_S model. First, we considered 1-D V_S models. To create these, we constructed a 1-D V_P model (Figure 3) by averaging the three-dimensional V_P of Arnulf et al. (2018) and then obtained one-dimensional V_S models by applying a set of 17 plausible depth-dependent V_P/V_S models (Figure S1 in the supporting information). Second, we applied the same set of depth-dependent V_P/V_S models to the 3-D V_P model to obtain a set of 3-D V_S models in which V_P/V_S was a function of depth. Third, we combined the 1-D V_P model with each 1-D V_S models to define V_S as a function of V_P and then applied these relationships to the 3-D V_P model to obtain a set of 3-D V_S models in which V_P/V_S is dependent on V_P. We performed inversions using each set of starting V_S models with V_P fixed during the inversions (Figure S2) by applying a large regularization weight to the 3-D V_P model.

For the three types of starting V_S models, we were able to find V_S models that yielded to similar reductions in *S* wave arrival time RMS residuals (Figure S2). However, for the second and third types of models, the hypocenters on the western side of the caldera consistently aligned along an apparent fault zone with a relatively small dip angle (~40°; Figures S2a and S2b). This dip angle is inconsistent with the steeply dipping caldera faults (>60°) typical observed in lab experiments (Folch & Martí, 2004; Geyer et al., 2006), on other volcanoes (e.g., Rabaul, Papoua New Guinea; Pinatubo, Philippines, Acocella, 2007) and with focal mechanisms nodal planes orientations for Axial Seamount (Levy et al., 2018). In contrast, hypocenters resulting from the 1-D starting V_S model showed more reasonable dips (>50°). Moreover, the hypocenters tend to be more clustered in this region for this inversion (Figure S2c), and thus more consistent with earthquakes in narrow fault zones. The primary features of the final V_P and V_S anomalies resulting from these tests are all very similar, suggesting that the starting V_S model has only a small influence on the final variations. We selected the 1-D V_S model as best type of starting model.

The selection of the preferred starting 1-D V_S model (Figures 3 and S1) was based on analyzing a large number of feasible models with decreasing V_P/V_S ratios with depth. Because there is a tendency for some earthquakes to locate below the roof of the magma chamber reported by Arnulf et al. (2014, 2018), we selected a model with relatively low V_S since this would favor shallower focal depths. Using the preferred starting model, we inverted the data to obtain our final both V_P and V_S variations by setting the regularization parameters to zero (Table 1). We tested other starting 1-D V_S models in such inversions and found that the inversions converged to similar velocity models with similar RMS travel time residuals, and only small differences in average focal depth.

4.2. Checkerboard tests

We explored the spatial resolution of our models using checkerboard tests. These tests also allowed us to determine the optimal regularization and smoothing parameters (Table 1). We considered checkerboards with cubic anomalies with dimensions ranging from 0.5 km to 2 km, with alternating ±10% variations applied to the final V_P and V_S models. Synthetic travel times were then computed through these synthetic models, and the data inverted using LOTOS after adding random Gaussian noise to both P and S travel times, with a standard deviation of 0.03 and 0.05 s, respectively, to simulate the uncertainties inferred from the RMS travel time residuals of the inversion.

The results show that the inversions are unable to resolve velocity anomalies with dimensions smaller than 1 km. Figures 4 and 5 show results for V_P and V_S, respectively, for a checkerboard with 1 km^3 anomalies, with a boundary at 0.5 km depth. The checkerboard patterns are resolved from the surface to a depth of 2 km. The best lateral resolution is obtained beneath the southeastern part of the caldera where density of rays is high (Figure 2). Amplitudes of V_S anomalies (Figure 5) are almost fully recovered (maximum recovery ~80%) for the best resolved bins. Amplitudes of V_P anomalies (Figure 4) are less well recovered (maximum recovery ~50%). When the checkerboards bins were shifted by 0.5 km vertically (Figures S3 and S4), similar results were obtained, with slightly better recovery for V_P amplitudes. From these tests, we are confident that the inversions can resolve long wavelength velocity anomalies above the magma chamber in the southern half of the caldera.

Because the recovered amplitude of V_S anomalies tends to exceed that of V_P, there is a tendency for V_P/V_S to increase in low-velocity regions and to decrease in low-velocity regions (Figure S5). However, in inversions that start with a good 3-D *P* wave velocity model, the under recovery of V_S anomalies might lead to the opposite effect.

4.3. Locations

To relocate the full catalog of 107,130 earthquakes with or final V_P and V_S models, we used the non-linear location package (NLLoc; Lomax et al., 2000). We first computed travel time grids for each stations by solving the eikonal equation using finite differences (Podvin & Lecomte, 1991). We then used the octree method from NLLoc to find the grid node associated with the highest probability. In contrast to LOTOS and other standard location algorithms (e.g., Hypo71 (Lee & Lahr, 1975) or HYPOINVERSE (Klein, 2002)), NLLoc performs a complete mapping of the earthquake location probability density function resulting in reliable error estimates. The smallest bin used in our grid search is a 12 m × 12 m × 12 m cube (X × Y × Z). Unlike LOTOS, it is possible to assign weights to individual picks in the forms of P and S arrival time uncertainties. We estimated an a posteriori error, σ_t for a fully weighted arrival time according to

$$\sigma_t = \sqrt{\sum_{i=1}^{N} \delta t_i^2 w_i^2 \Big/ \sum_{j=1}^{M} (n_j - p)}, \tag{1}$$

where δt_i and w_i are the travel time misfits and weights, respectively, of the N arrival times used for all the locations, n_j are the number of arrival times for each of the M earthquakes located, and p is the number of free parameters for each earthquake location and is set to 4.

5. Results

5.1. Residuals Improvements

Figure 6 shows the evolution of the *P* and *S* wave residuals during the joint inversion. The final 3-D velocity models were obtained after four iterations with the travel time RMS residuals stable after two iterations (Figure 6a). Eastern stations (except AXID1) have a bigger influence on the joint inversion than western stations because they are associated with more P and S picks (Figure 6b). The RMS residuals for the 3-D model are substantially reduced from the 1-D model (Figures 6c–6g), changing from 0.040 to 0.033 s for *P* waves (32 % variance reduction) and from 0.103 s to 0.049 s for *S* waves (77 % variance reduction). The 3-D inversion leads to distribution of residuals that are approximately Gaussian with a zero mean and with far fewer large *S* wave residuals than for the 1-D model (Figures 6f and 6g). The final residuals are similar on all the seven

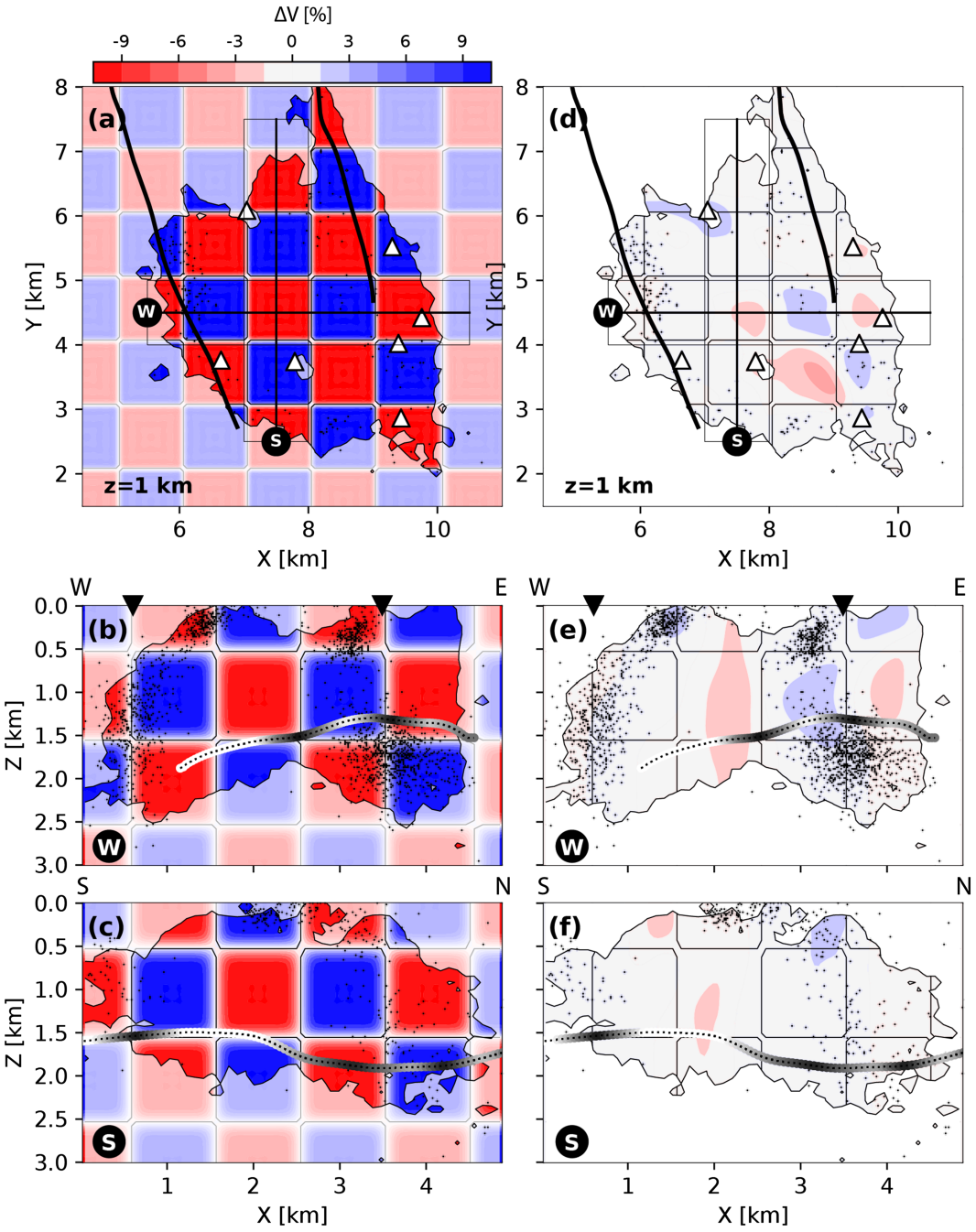

Figure 4. Results of the synthetic checkerboard test applied to the final 3-D V_P model. (a–c) The starting checkerboard comprises 1 km^3 cubes with ±10% variations applied. Random noise with a standard deviation of 0.03 s was added to the synthetic P onset times. (d–f) Inversion results after four iterations using LOTOS. Bright areas in a–c indicate the mask used based on ray-density (a threshold of two rays/bin). Earthquake locations shown as dots are those obtained after four iterations (dots). Cross-sections (b and c) and (e and f) use a maximum projection distance of 0.5 km. The stations and the top of the magma are shown using the same convention as in Figures 1 and 2.

stations with the reduction in *S* wave residuals particularly large for the stations located on the western side (AXAS1 and AXAS2) and center of the caldera (AXCC1), which are fit poorly by the 1-D model (Figure 6c). Earthquakes tend to be more clustered from one iteration to another and locations are stable after two iterations (Figure S6)

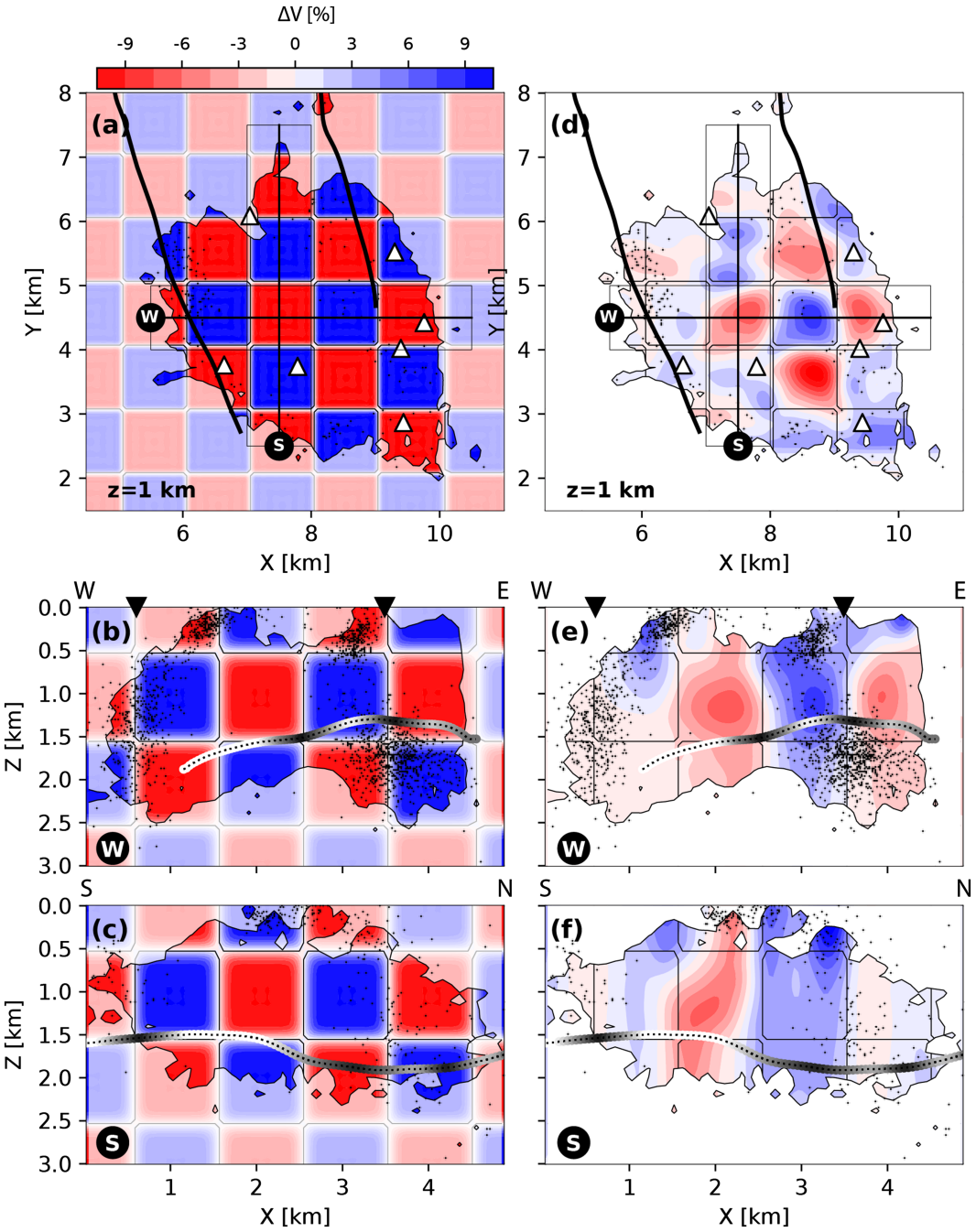

Figure 5. Results of the synthetic checkerboard test applied to the final 3-D V_S model plotted using the same convention as in Figure 4. Random noise with a standard deviation of 0.05 s was added to the synthetic S onset times.

5.2. 3-D Velocity Models

Figure 7 shows the velocity perturbations from the average 1-D velocity profiles (shown in Figure 3) for the starting V_P model and the final V_P and V_S models (Figure S7 shows the absolute velocities of all three models for comparison). The inversion reveals a number of interesting features that the checkerboard test suggest are well resolved (i.e., features that are ≥ ~1 km^3).

The starting and final V_P models show similar broad scale variations, supporting the idea that the starting V_P model, derived from active source data inversions, is a good approximation of the true velocity model

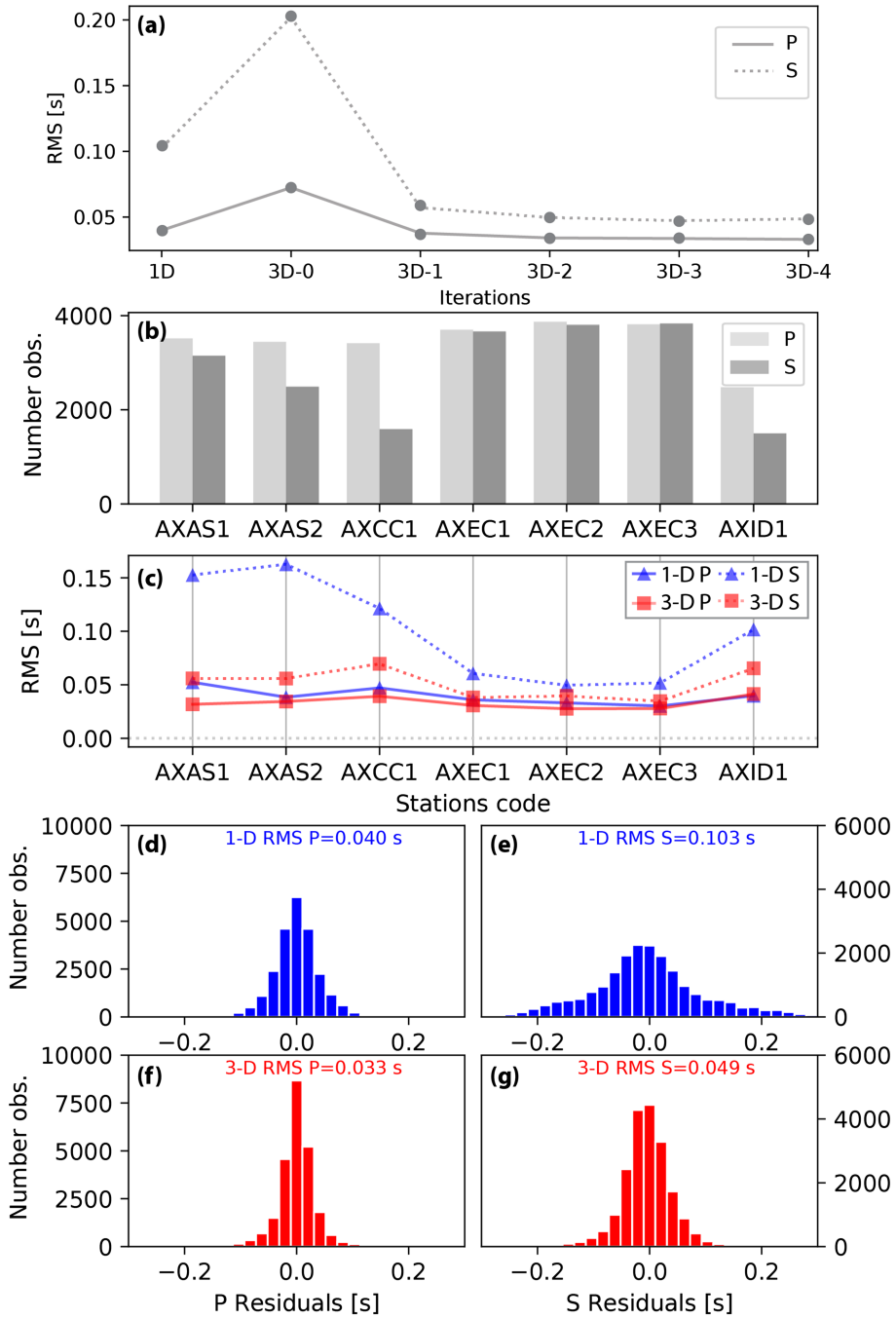

Figure 6. Evolution of travel time RMS residuals associated with the LOTOS joint inversion procedure. (a) RMS residuals for *P* and *S* waves using the 1-D V_P and *Vs* models (from Wilcock et al., 2016) and evolution for the four iterations using the 3-D V_P and *Vs* models (solid and dashed lines, respectively). RMS residuals are stable after two iterations and fully converge after four iterations. (b) Number of *P* and *S* observations per station (station names are shown in Figure 1). (c) RMS residuals for *P* and *S* waves using the 1-D V_P and *Vs* models (blue) and using the final 3-D V_P and V_S models (red). Distribution of P residuals (d) and S residuals (e) using the 1-D models. (f–g). As for (d–e) except for the final 3-D models.

(Figure S8). These similarities include a low-velocity anomaly in the middle of the imaged southern half caldera and a low-velocity anomaly along the eastern wall of the caldera (Figures 7a–7h). The similarity is particularly strong at shallow depths (Figures 7a and 7e) where the models are primarily constrained immediately below the OBSs. At greater depths, the low-velocity along the eastern wall (B2 on Figures 7b

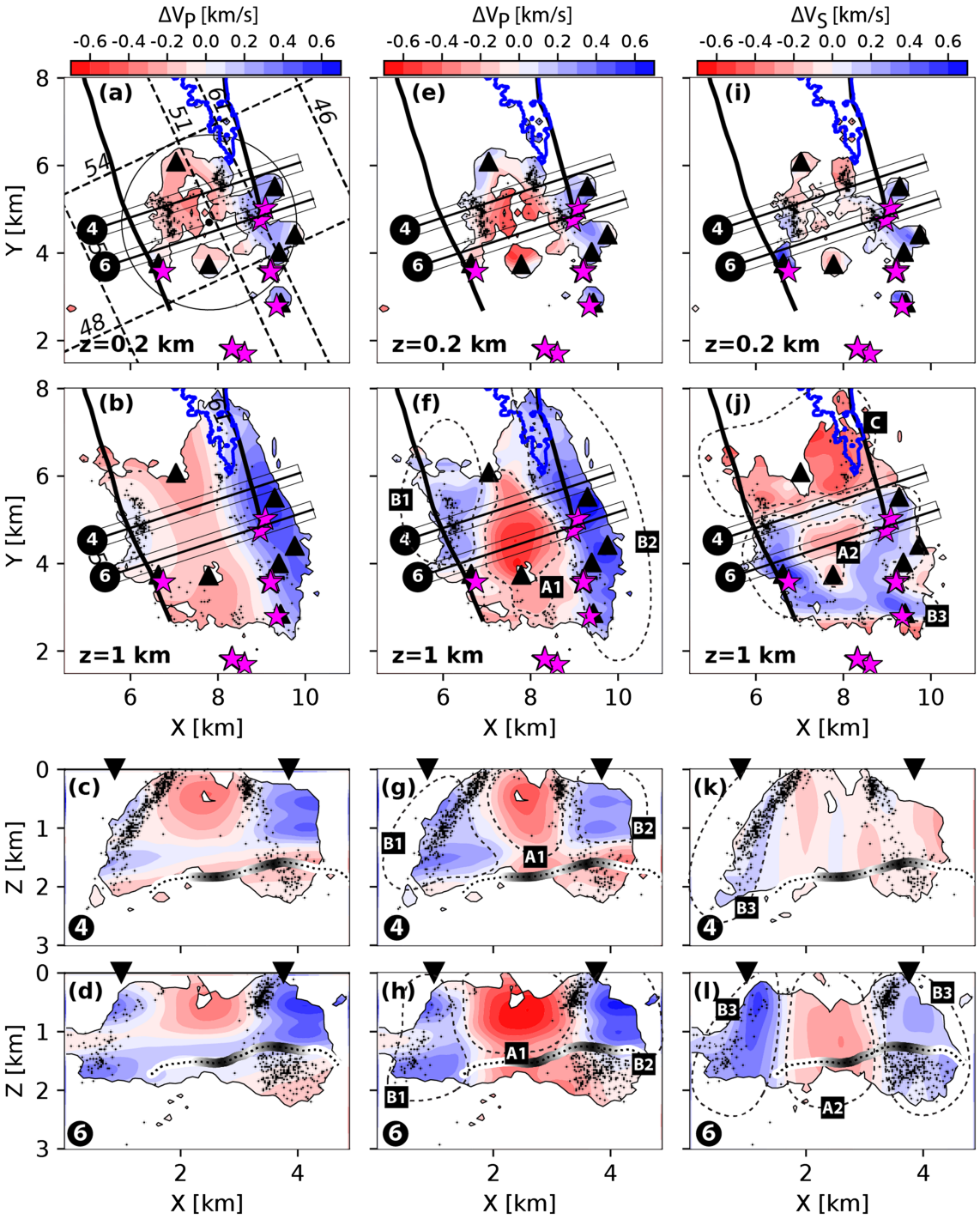

Figure 7. 3-D velocity anomalies relative to the average 1-D profiles computed by averaging velocities horizontally inside the circle shown on (a). (a–d) ΔV_P of the starting model (Arnulf et al., 2018); (e–h) ΔV_P of the final model after four iterations; (i–l) ΔV_S of the final model after four iterations. Depth sections are shown at 0.2 km and 1 km depth. Cross-sections use a maximum projection distance of 0.2 km for earthquakes and are labelled 4 and 6 so that they correspond the same numbered section in Figure 10. The color scale is centered on 0 and identical for V_P, V_S variations for better comparison. The mask applied is based on ray-density (threshold at two rays/bin). The main anomalies are highlighted by dashed labeled contours and are labelled A1–A2, B1–B3, and C. Caldera walls, lava flows, vent fields, seismic lines and top of the magma chamber are shown using the same conventions as in Figures 1 and 2. Stations are represented by black triangles for clarity.

and 7f) is similar in both models with a maximum anomaly ~11% higher than the mean 1-D profile. However, elsewhere at depth, the models differ significantly, and the final V_P model has larger anomalies. The low-velocity anomaly sitting in the caldera (A1 on Figures 7f–7h) is more pronounced in the final V_P

model (~15% slower than the mean 1-D profile) than in the starting V_P model (Figures 7b–7d; ~6% slower) and is characterized by a single minimum that sits between two minima in the starting model. In the final model, the anomaly is ~2 km wide in the east-west direction and appears to be bounded by the outward-dipping ring faults (Figures 7f and 7g). The north-south extent of this anomaly is less well constrained due to ray coverage. However, the anomaly has a smaller north-south extent in the final V_P model than in the starting V_P model and is estimated to be ~3 km long. In the final model, the low velocities extend to greater depths and appear to reach the magma chamber at 1.6 to 2 km depth (Figures 7g and 7h). Another striking difference between the starting and final V_P models is the low-velocity anomaly underlying the western caldera wall (B1 on Figures 7f–7h). In the final model, this anomaly correlates well (both horizontally and vertically) with the western outward-dipping ring fault drawn by hypocenters (Figure 7g) with velocities ~8% higher than the mean 1-D profile. In contrast, this anomaly is discontinuous and much weaker in the starting model (Figures 7b–7d; ~4% higher).

The pattern of final velocity anomalies for V_S differs in many ways from that for V_P. The V_S model includes a circular low-velocity anomaly in the center of the southern part of the caldera (A2 on Figures 7j and 7l). This anomaly has a diameter of ~1 km, falling within the resolution of our model, and connects to the top of the magma chamber. Contrary to the V_P model, this low-velocity anomaly appears to be completely surrounded by a low-velocity anomaly (B3 on Figures 7j–7l; ~21 % higher than the mean 1-D profile), although the northern part of this anomaly, crossing the caldera from east to west, is <1 km wide and may not be well resolved. Towards the north of the caldera, we observe a large low V_S anomaly (C on Figure 7j; ~20% slower), extending across the caldera and beneath the eastern caldera wall. The southernmost portion of this anomaly is well resolved and extends to a depth of ~2 km. This anomaly has no counterpart in the V_P model.

V_P/V_S ratios (Figure 8) show large horizontal variations, especially at shallow depths. At 0.2 km depth V_P/V_S ranges from 1.5 to 3.2 and is particularly low under the westernmost station which coincides with the ASHES vent field (Figure 8a). At depths $\geq$ ~0.5 km (Figure 8b), the southern caldera is underlain by an extensive region of low V_P/V_S. In the ring corresponding to high V_S (B3 on Figures 7j–7l), V_P/V_S is particularly low and here $V_P/V_S < 1.9$ extends to greater depth than in the center of the anomaly (Figure 8d). This region of deeper low V_P/V_S coincides with the location of hypocenters defining the outward-dipping faults (Figures 8c and 8d). V_P/V_S is markedly higher to the north (Figure 8b) in the region corresponding to low V_S (C on Figure 7j). The transition between low and high V_P/V_S to the north is quite sharp (Figure 8b), particularly on the east side of the caldera, and corresponds to the southern extend of the 2015 lava flows.

5.3. Locations Comparisons

The joint inversion yields a velocity model that can be used to relocate all the seismicity, but this is done with a different algorithm. In order to understand the effects of using 3-D instead of 1-D velocity models for locations and using NLLoc instead of LOTOS, we quantitatively compared locations of the earthquake data set used in the inversion. Figure 9 shows the residual distributions for *P* and *S* waves and cross-sections of hypocenter locations for different sets of models and algorithms. Using the final 3-D models instead of the 1-D models and LOTOS (Figures 9a and 9b and 6d–6g) considerably reduces the residuals, from 0.040 to 0.033 s for *P* waves and from 0.103 to 0.049 s for *S* waves. In cross-section, it can be seen that going from 1-D to 3-D has a substantial effect on locations, with shallower locations and more clearly defined faults. Using the final 3-D models but using NLLoc instead of LOTOS (Figures 9b and 9c) ,we see that the residuals are slightly smaller for *P* waves (0.029 versus 0.033 s) and larger for *S* waves (0.066 versus 0.049 s). This is presumably a result of the different ray tracers used in the two algorithms and the more sophisticated weighting scheme used in NLLoc that reduces the average weight and thus, the fit of *S* wave travel times. In cross-section, locations are comparable, with earthquakes appearing more clustered and deep earthquakes slightly shifted upwards when using NLLoc instead of LOTOS. Using the final 3-D V_P model but an averaged 1-D V_S model instead of a 3-D V_S model and NLLoc (Figures 9c and 9d), we see that the residuals for *P* waves are similar (0.033 versus 0.029 s) but considerably larger for *S* waves (0.140 versus 0.066 s). In cross-section, earthquakes appear clustered but the faults are not well defined. The shift in locations between 3-D and 1-D V_S models can exceed 0.5 km even within the network (Figure S9). This result shows the importance of using a 3-D V_S model instead of a 1-D V_S model.

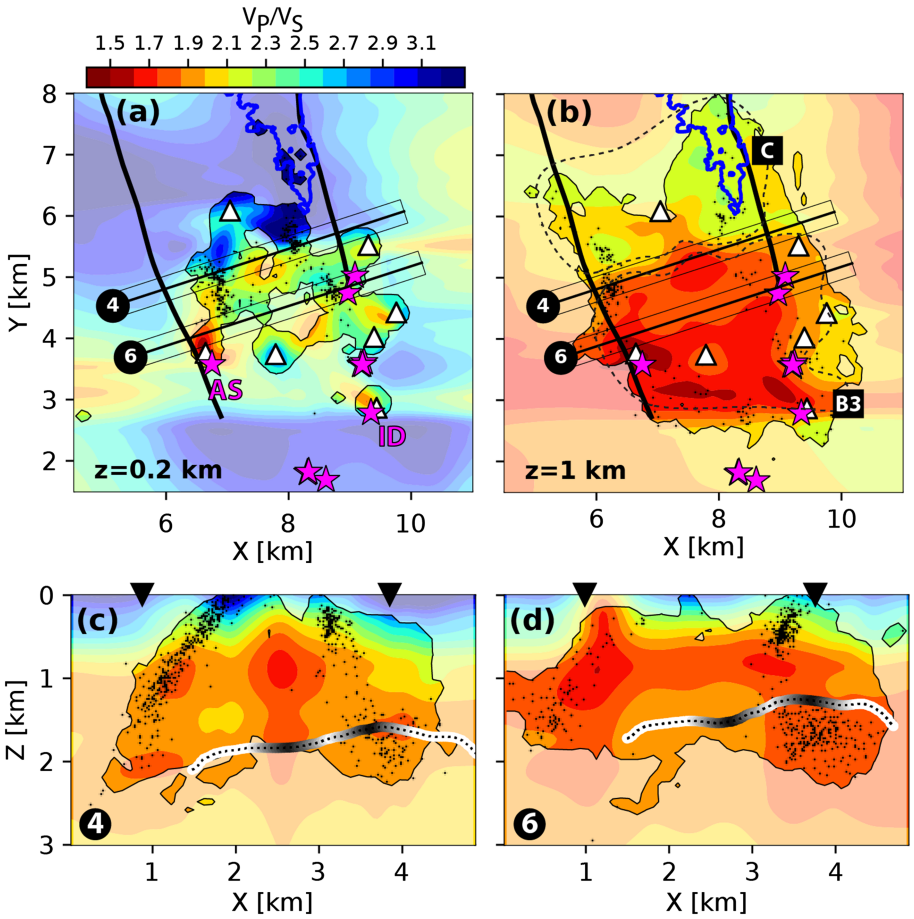

Figure 8. Final 3-D V_P/V_S model obtained after four iterations. Depth sections are at (a) 0.2 km and (b) 1 km depth and (c–d) cross-sections use a maximum projection distance of 0.2 km for earthquakes. The main anomalies are highlighted by dashed labeled contours. Stations, caldera walls, lava flows, vent fields, seismic lines, and top of the magma chamber are shown using the same convention as in Figures 1 and 2.

5.4. Final Catalog

We relocated the 107,130 earthquakes in the HYPOINVERSE catalog using NLLoc and the final 3-D V_P and V_S models. To eliminate unreliably located earthquakes, we only kept those that have 10 or more weighted phase recordings, which resulted in a catalog of 76,512 earthquakes (Figure 10). The *a posteriori* error calculated using equation (1) is 0.029 s, and the median formal 1-σ uncertainties for the locations are 0.16 km for longitude, 0.15 km for latitude, and 0.26 km for depth. Compared to the locations obtained with HYPOINVERSE using 1-D velocity models (Figure S10; Wilcock et al., 2016), the newly located earthquakes are shallower and delineate clusters that were only poorly defined in the initial catalog (Figures S11 and S12). In Figure 10, we label six noticeable clusters, two to the West (W1-2), three to the East (E1-3), and one to the South (S1). Figure 11 shows earthquake density on a logarithmic scale.

Cluster W1 delineates the northern portion of the western outward-dipping ring fault. Its dip is estimated to be ~50° on Profiles 3 and 4 (Figures 10 and 11). Cluster W2 delineates the southern part of the western ring fault and includes more earthquakes than cluster W1 and. On Profiles 5 and 6, it shows a noticeable change in fault dip from ~30° at depths shallower than ~0.5 km to ~45° at higher depths.

Cluster E1 forms the northern part of the eastern ring fault. Despite the relatively sparse distribution of earthquakes, the cluster is consistent with a subvertical outward-dipping ring fault (~78°). This cluster follows the trend of 2015 eruptive fissures with shallower earthquakes closer to the eastern caldera wall to

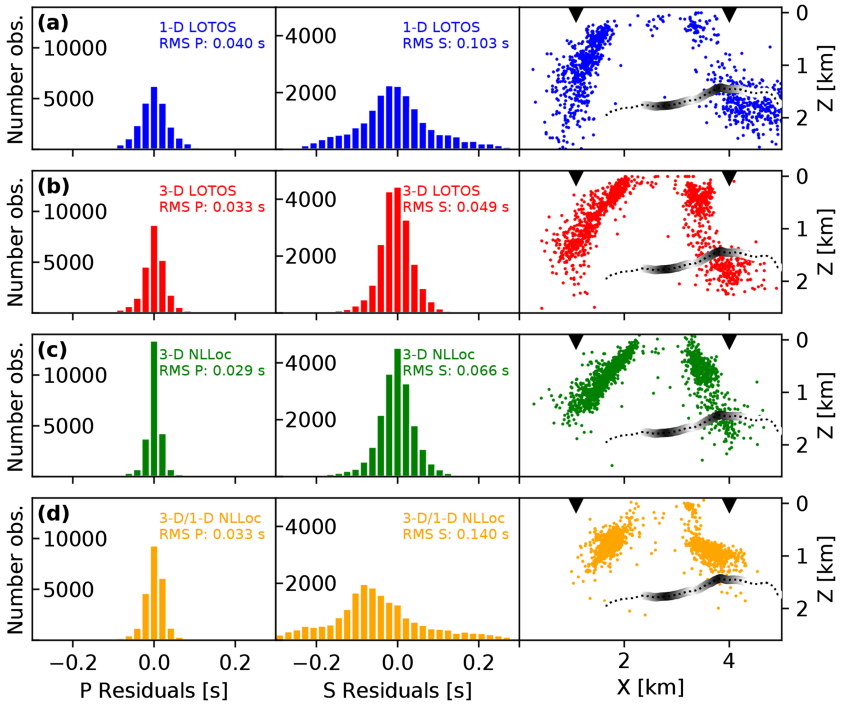

Figure 9. *P* and *S* time residuals and earthquake locations comparisons for different velocity sets and algorithms showing results from (a) LOTOS and 1-D V_P and 1-D V_S models, (b) LOTOS and the final 3-D V_P and 3-D V_S models, (c) NLLoc and the final 3-D V_P and 3-D V_S models, and (d) NLLoc and the final 3-D V_P model and the averaged 1-D V_S model. Earthquake locations are projected up to 0.8 km onto Profile 4 shown on Figure 1. The caldera walls and the top of the magma chamber are shown using the same convention as in Figure 2.

the north. Cluster E2 includes the largest number of earthquakes and is mostly limited to ≤1 km depth. A striking feature of this cluster is a change in the dominant dip direction from north to south, which is particularly apparent on the earthquake density plots (Figure 11). On Profile 4, where it merges into cluster E1, and Profile 5, the dip is ~50° to the east consistent with the outward-dipping ring fault while on Profiles 6 and 7, the dip is ~80° to the west consistent with a steep inward-dipping fault that connects to the eastern caldera wall, eruptive fissures, and hydrothermal vents. Clusters E1 and E2 are noticeably broader than clusters W1 and W2. Cluster E3 underlies E2 and delineates the deeper portion of the outward-dipping eastern ring fault in the southern caldera. Moving south, cluster E3 becomes denser while the overlying cluster E2 progressively fades (Profiles 8 and 9).

Cluster S1 comprises three nearby subclusters in the southernmost part of the caldera. This cluster is diffuse and does not show any clear dip on E-W or N-S profiles (Figures S13 and S14). There are also a significant number of earthquakes outside the clusters. The densest concentration is a broad band of shallow earthquakes (<0.5 km) connecting the western and eastern clusters in the center of the southern half of the caldera (Profiles 4–6).

6. Discussion

6.1. Velocity Anomalies

The joint inversion of earthquake arrival times for velocity and hypocenter parameters is a challenging problem because it is inherently non unique (Pavlis & Booker, 1980). For our problem, we had the advantage of a good starting 3-D V_P model derived from inverting active source seismic data. Also in contrast to prior joint inversions that solved for V_P and V_S on MORs (Barclay et al., 2001; Barclay & Wilcock, 2004), where most of the earthquakes were located at a similar midcrustal depth in a single region that was relatively restricted along axis, the earthquakes in our inversion are concentrated at a range of depths on two distinct faults. This ensures a better distribution of crossing ray paths although with only seven OBSs, the distribution of

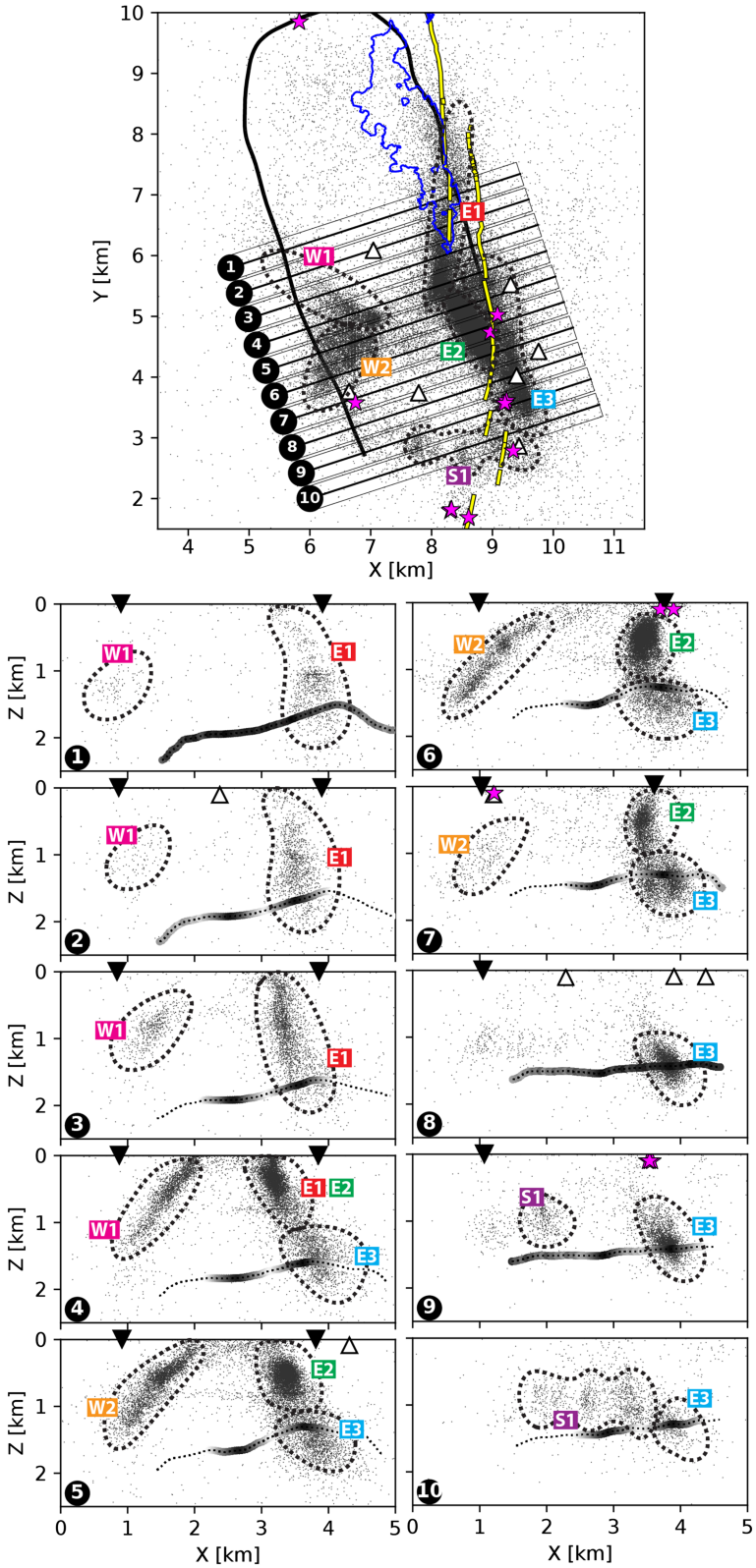

Figure 10. Locations of 76,512 earthquakes having 10 or more phase recordings (71% of the total number of earthquakes in the HYPOINVERSE catalog (Wilcock et al., 2017). Locations were obtained using NLLoc and the final 3-D V_P and V_S models. Cross-sections use a maximum projection distance of 0.2 km for earthquakes. Six clusters of earthquakes are clearly identified, two to the West (W1-2), three to the East (E1-3) and one to the South (S1). Stations, caldera walls, lava flows, vent fields, and top of the magma chamber are shown using the same convention as in Figures 1 and 2.

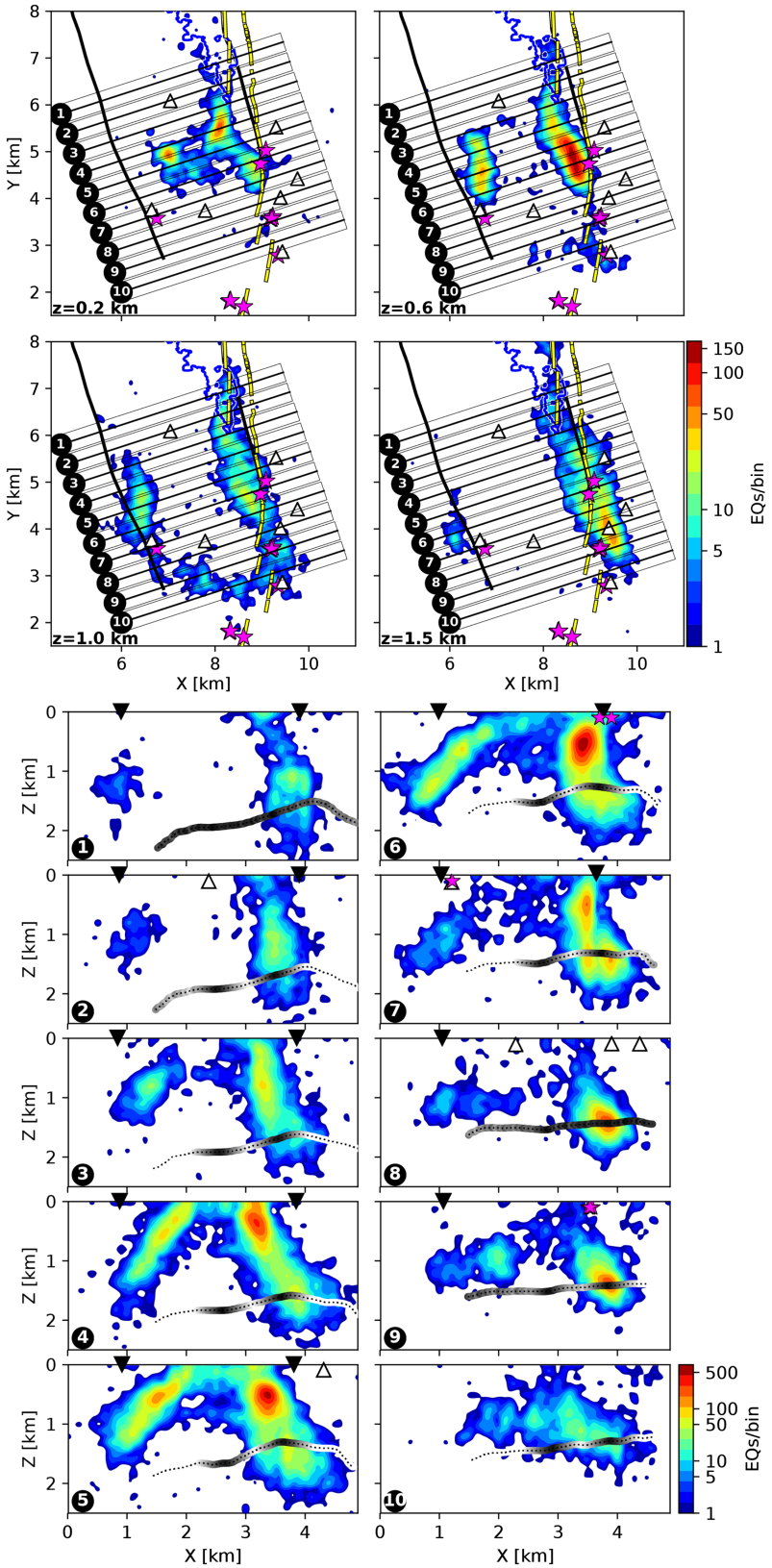

Figure 11. Depth-sections and cross-sections showing density per 0.1 km × 0.1 km × 0.1 km bin with a logarithmic color scale for the 76,512 earthquakes of Figure 10. Depth-sections are given at depth 0.2, 0.6, 1, and 1.5 km, and cross-sections parameters are as for Figure 10. Stations, caldera walls, lava flows, vent fields, and top of the magma chamber are shown using the same convention as in Figures 1 and 2.

ray paths is still limited particularly in the uppermost crust. We proceeded by selecting an initial subset of well-recorded earthquakes and showed that the final residuals and velocity models are insensitive to the starting V_S model. Checkerboard tests showed that our final 3-D V_P and 3-D V_S models can resolve features that have a dimension of 1 km and to a depth of ~2 km in the southern half of the caldera. LOTUS does not provide capability to apply a penalty function or smoothing directly to V_P/V_S, so observed anomalies likely deviate beyond realistic ranges. Nevertheless, considering the large spatial scale and high amplitude of the primary V_P/V_S anomalies, these features are likely real and worthy of interpretation even if the absolute values are incorrect.

The most prominent low-velocity anomaly is located in the middle of the caldera (A1 and A2 on Figure 7) that connects to the magma chamber at ~1.6 km depth. This low V_P and V_S anomaly requires that the pillow basalts and sheeted dikes of Layer 2 are associated with high porosity and fracturing and possibly hydrothermal alteration. Intense fracturing in the southern caldera is likely to result from the repeated cycles of inflation and deflation of the underlying magma chamber (Nooner & Chadwick, 2016). The magma chamber is shallowest in this region, and the southern and particularly southeastern caldera is clearly a focus of magmatism and deformation as evidenced by the pattern of magma emplacement (Chadwick et al., 2013), the inferred region of magma resupply (Nooner & Chadwick, 2016), and the rates of seismicity (Wilcock et al., 2016).

The rim of the caldera is characterized by high V_P and V_S (B1, B2, and B3 on Figure 7). Similar anomalies are observed in other calderas such as Campi Flegrei (Vanorio et al., 2005; Zollo et al., 2003) and Deception Island (Zandomeneghi et al., 2009) where they are interpreted as consolidated/frozen lava flows that fed earlier eruptions and that are less subject to inflation/deflation deformations. These relatively low-velocity anomalies are also influenced by the variations in Layer 2 thickness due to subsidence of the caldera and ponding of lavas within the caldera. Arnulf et al. (2018) report that Layer 2A thickens from 0.4–0.6 km on the rim to 0.75–0.95 km inside the caldera.

At 1 km depth, the southern part of the velocity model is characterized by a broad region of low V_P/V_S that extends across both the high and low-velocity anomalies. At this depth, values below 1.7 are observed around the southern edge of the caldera and this extend to the surface at ASHES vent field. Low V_P/V_S can be indicative of a medium that is cut by low aspect ratio (fat) cracks (e.g., Kim et al., 2018), but it is not obvious why the crack geometry should be so different in this region. The low V_P/V_S values are also consistent with the presence of vapor in the system that can drastically lower V_P while having little effect on V_S (Toksöz, 1976). Butterfield et al. (1990) analyzed the fluids expelled at the ASHES hydrothermal vents and estimated the boiling point to be around 370 °C, which corresponds to a pressure of 250 bar or ~1 km below seafloor, consistent with the deeper limit of the low V_P/V_S anomaly observed (Figure 8d). We note that the inferred region of vapor coincides overlies the southern portion of the magma chamber, which is inferred to have the highest melt content (Arnulf et al., 2014) and is thus, consistent with a higher heat flux and higher temperatures in the overlying crust.

The low V_P/V_S anomaly immediately beneath the ASHES vent field (Figure 8a) may also indicate the presence of hydrothermal breccias. V_P/V_S as low as 1.55 was measured in the laboratory for microcores of silicified and chloritized breccias at 100 m below seafloor sampled at the TAG hydrothermal vent field (Ludwig et al., 1998). Breccias are characterized by a high concentration of large aspect ratio pore spaces rather than a high concentration of thin cracks than can increase V_S and lower V_P/V_S (Kim et al., 2018).

Another prominent feature is the low V_S anomaly and high V_P/V_S anomaly in the northern part of the model (C on Figures 7 and 8). The region mostly outside the seismic network but extends to within regions that the checkerboard tests suggest are at least partially resolved (compare Figure 7 with Figures 4 and 5). This anomaly has no counterpart in the V_P model indicating a change in the pore characteristics rather than a change in the type of fluids filling the medium (Sanders et al., 1995). This anomaly has deep roots, and the lowest V_S values correlate well with the location of the lava flows expelled during the 2015 eruption. Dike intrusion from the magma chamber to the surface may have impacted the surrounding rocks by creating a crack population dominated by thin cracks with high V_P/V_S (Kim et al., 2018) through the combined effects of fracturing during dike propagation and partial crack closure as the dikes accommodate strain.

The very high V_P/V_S ratio observed in the shallow part of this anomaly (maximum of 3.2 at ~0.2 km depth) may result from the combination of small aspect-ratio cracks and the fully saturated high porosity nature of the surface basalts. We note that V_P/V_S ratios >3 have been observed on other spreading centers (Christeson et al., 1997; Collier & Singh, 1998) and thus appear typical for Layer 2A in young oceanic crust.

6.2. Earthquakes Distribution

Some earthquakes locate below the top of the magma chamber in our final models, using either LOTOS (Figure 9) or NLLoc (Figures 9–11). Most of these are part of cluster E3 on the east side of the caldera (Figure 10, Profiles 4–9). In the LOTOS joint inversions, we tried to force these earthquakes shallower by selecting a starting model with relatively low V_S (Figure S1). However, the final locations are relatively insensitive to the starting velocity model. Thus, while earthquakes for the first iterations are mostly located near or above the top of the magma chamber, they are progressively located at greater depth through successive iterations (Figure S6), as the inversion globally increases the V_S model (Figure 3) to a final velocity solution that is largely independent of the starting model.

Only ~10% of the earthquakes are located below the top of the magma chamber (Figure S15), and this can be explained by two factors. First, the earthquake locations and the position of the top of the magma chamber interpreted from MCS reflection profiles (spline interpolation applied between profiles) have errors that, when combined, may be greater than the observed depth difference. Second, the magma chamber may be discontinuous and parts of the reservoir can be associated with lower melt fractions (Arnulf et al., 2018) allowing brittle failure thus generating earthquakes. Indeed, given that the deformation data require that magma chamber inflation is confined to a localized portion of the magma chamber underlying the southeastern caldera (Nooner & Chadwick, 2016), it is clear that the magma chamber is not a continuous region of well-connected melt.

As observed in previous studies that relocated earthquakes with 1-D velocity models (Levy et al., 2018; Wilcock et al., 2016) and a 3-D V_P model (Arnulf et al., 2018), the distribution of earthquakes under Axial Seamount defines, in map view, a figure eight pattern with high earthquake densities around the caldera and across its center (Figure S16), this pattern is truncated to the north by low earthquake densities in the northern caldera (Figure S16). However, our catalog differs in some significant ways. At the northern edge of the network, Arnulf et al. (2018) reported conjugate inward-dipping faults connecting to the caldera walls and dipping at ~40°–47°. We do not see inward-dipping faults in this region in our catalog (Figures 10, S13, and S14) even when we plot cross sections using the same conventions. Instead, we observe outward-dipping faults in this region (compare Profile 1 in Figures S13 and S14 with Figure 8e in Arnulf et al., 2018). Also, Arnulf et al. (2018) report that earthquakes on the western wall are concentrated in a band that is inclined to the south, but there is no similar pattern in our catalog (compare Profile 3 in Figures S13 and S14 with Figure 8c in their paper). Some of these differences may arise from the location algorithm. Whereas Arnulf et al. (2018) used a location algorithm based on shortest paths, we are using a more standard location algorithm NLLoc, which solves for the eikonal equation. However, the differences likely primarily reflect the use of a tomographic 3-D V_S model used here compared to a V_S model that is a scaled version of the 3-D V_P model as used in Arnulf et al. (2018).

Within the network in the central part of the caldera, all studies observe conjugate outward-dipping faults but with different dips than can be attributed to the different location algorithms and velocity models used and also possibly to projection artifacts (i.e., projecting earthquakes relatively large distances onto planes that are not quite orthogonal to the fault structures). In our catalog, the eastern clusters define an outward-dipping fault (~50°) that changes to a subvertical inward-dipping fault (~80°) connecting to the caldera wall and vent fields moving south (Profiles 4–7 in Figures 10 and 11). This inward-dipping fault is not clearly observed in other studies but is consistent with some focal mechanisms having subvertical nodal planes (Levy et al., 2018), and earthquakes could be linked to the pathways of hydrothermal fluid beneath the easternmost vent fields. We note that the eastern clusters are also generally wider than the western clusters even though these are more centrally located within the network and thus presumably better resolved. We infer that the earthquakes beneath the eastern wall are indicative of multiple faults in a wide damaged zone.

Another interesting feature is the break in the slope observed on the southwesternmost cluster (W2 on Figure 10), this change in slope is not clearly observed in other studies and may indicate the root of an aseismic inward-dipping fault connecting to the west caldera wall. The generally lower fault dips observed on the western wall in this (Figures 10 and 11) and prior studies (Arnulf et al., 2018; Wilcock et al., 2016) may also reflect a ring fault system adjusting to movement of the magma chamber that is now offset to the east of the caldera (Figure 1), presumably because of the eastward migration of the Cobb-Eickelberg hotspot relative to the JdFR (Arnulf et al., 2018).

Finally, Cluster S1 coincides with the southern tip of the caldera and might indicate motion in a zone of deformation that connect the outward-dipping faults on the east and west wall into a continuous ring fault system. The caldera appears to be hinged in this region, which may explain the relatively low rates of seismicity (i.e., limited deformation) and the absence of a single fault structure with a clearly resolved dip. Alternatively, since seismicity rates remained relatively high in this region following the 2015 eruption (Wilcock et al., 2018), the earthquakes may be related to ongoing hydrothermal processes (Sohn et al., 2004).

7. Conclusion

We use data from the OOI Cabled Array seismic network that spans the southern portion of the Axial Seamount caldera, for a joint inversion of ~3900 well recorded earthquakes for hypocentral parameters and 3-D V_P and V_S. The velocity models are then used to relocate >76,000 earthquakes with at least 10 arrival time observations. Although, joint hypocentral locations are often nonunique, the primary feature in the final V_P and V_S models is insensitive to the starting model, and checkerboard tests suggest that the spatial resolution within the network is ~ 1 km in all directions, allowing the interpretation of the structure underneath the caldera to the depth of the Axial Magma chamber at ~2 km depth. The final 3-D V_P model resulting from our passive tomography differs only slightly from the starting 3-D V_P model obtained by Arnulf et al. (2018) from active source data. In contrast, the final 3-D V_S model differs significantly from the starting 1-D V_S model and models obtained assuming V_S is a uniform function of V_P indicating that the V_S structure is highly heterogeneous. The final 3-D velocity models reduce the variance of *P* wave and *S* wave arrivals by 32 % and 77 % compared locations obtained with 1-D velocity models.

The velocity models resolve a number of interesting features. A prominent low V_P and V_S anomaly in the center of the caldera is attributed to existence of porous rocks, fractured by repeated inflation/deflation cycles of the magma chamber and possibly altered by hydrothermal circulation. High V_P and V_S around the caldera rim is likely due to consolidated, undeformed lava. The southern end of the caldera is underlain by a broad region of relatively low V_P/V_S that extends to 1 km depth and is consistent with the presence of hydrothermal vapor. Low V_P/V_S at shallow depths below ASHES hydrothermal vent field may result from vapor and/or hydrothermal breccias. A region of low V_S and high V_P/V_S in the northern part of the caldera lies mostly outside the seismic network and may indicated the presence of thins cracks in a region influenced by diking.

The relocated earthquakes clearly image the outward-dipping ring faults, revealing shallow and well-defined clusters. The inward-dipping ring faults reported by Arnulf et al. (2018) to the north of the network for locations obtained with the 3-D active source tomography *P* wave model and a simple V_S (V_P) function are not observed when an independent 3-D *S* wave model is used. However, within the network, we observe a steep inward-dipping fault connecting to the eastern caldera wall.

Our study included data from only seven cabled OBSs but shows the value of joint inversions for hypocentral parameters and 3-D V_S and V_P at MOR sites where an active-source tomographic *P* wave model exists and where the earthquake distributions lead to crossing ray paths. If the Axial cabled seismic network was enhanced by data from a temporary deployment of autonomous OBSs during an interval of high seismicity, we suggest that the spatial extent and resolution of the velocity models and the accuracy of earthquake locations could be further improved.

Acknowledgments
We thank Ivan Koulakov for his extensive guidance on the use of LOTOS, and Milena Marjanović, an anonymous referee and Associate Editor Greg Waite for thoughtful reviews. The starting 3-D *P* wave velocity model (Arnulf et al., 2018, doi: 10.1594/IEDA/324420) and initial hypocentral earthquakes locations for the 2015 Axial Seamount eruptive sequence (Wilcock et al., 2017; doi:10.1594/IEDA/323843) can be found on the Marine Geoscience Data System. The final 3-D *P* and *S* wave velocity models (Baillard & Wilcock, 2019a; doi:10.1594/IEDA/324821) and catalog of relocated earthquakes (Baillard & Wilcock, 2019b; doi:10.1594/IEDA/324822) resulting from this study are also available in the Marine Geoscience Data System. This research was funded by National Science Foundation (grants OCE-1536219, OCE-1536320, OCE-1357076, and OCE-1658199).

References

Acocella, V. (2007). Understanding caldera structure and development: An overview of analogue models compared to natural calderas. *Earth-Science Reviews*, *85*(3–4), 125–160. https://doi.org/10.1016/J.EARSCIREV.2007.08.004

Arnoux, G. M., Toomey, D. R., Hooft, E. E. E., & Wilcock, W. S. D. (2019). Seismic imaging and physical properties of the endeavour segment: Evidence that skew between mantle and crustal magmatic systems governs spreading center processes. *Geochemistry, Geophysics, Geosystems*, *20*, 1319–1339. https://doi.org/10.1029/2018GC007978

Arnulf, A. F., Harding, A. J., Kent, G. M., Carbotte, S. M., Canales, J. P., & Nedimović, M. R. (2014). Anatomy of an active submarine volcano. *Geology*, *42*(8), 655–658. https://doi.org/10.1130/G35629.1

Arnulf, A. F., Harding, A. J., Kent, G. M., & Wilcock, W. S. D. D. (2018). Structure, seismicity, and accretionary processes at the hot spot-influenced axial seamount on the juan de fuca ridge. *Journal of Geophysical Research: Solid Earth*, *123*, 4618–4646. https://doi.org/10.1029/2017JB015131

Arnulf, A. F., Singh, S. C., Harding, A. J., Kent, G. M., & Crawford, W. (2011). Strong seismic heterogeneity in layer 2A near hydrothermal vents at the Mid-Atlantic Ridge. *Geophysical Research Letters*, *38*, L13320. https://doi.org/10.1029/2011GL047753

Baillard, C., Crawford, W. C., Ballu, V., Hibert, C., & Mangeney, A. (2014). An automatic kurtosis-based P- and S-phase picker designed for local seismic networks. *Bulletin of the Seismological Society of America*, *104*(1), 394–409. https://doi.org/10.1785/0120120347

Baillard, C., & Wilcock, W. S. D. (2019a). Three-dimensional P- and S-wave velocity models for Axial Seamount from a joint inversion of earthquake arrival times for velocity and hypocentral parameters. *Interdisciplinary Earth Data Alliance*. https://doi.org/10.1594/IEDA/324821

Baillard, C., & Wilcock, W. S. D. (2019b). Catalog of earthquakes at Axial Seamount relocated with three-dimensional P- and S-wave velocity models from a joint inversion of earthquake arrival times for velocity and hypocentral parameters. *Interdisciplinary Earth Data Alliance*. https://doi.org/10.1594/IEDA/324822

Barclay, A. H., Toomey, D. R., & Solomon, S. C. (2001). Microearthquake characteristics and crustal V P/V S structure at the Mid-Atlantic Ridge, 35°N. *Journal of Geophysical Research*, *106*(B2), 2017–2034. https://doi.org/10.1029/2000JB900371

Barclay, A. H., & Wilcock, W. S. D. (2004). Upper crustal seismic velocity structure and microearthquake depths at the Endeavour Segment, Juan de Fuca Ridge. *Geochemistry, Geophysics, Geosystems*, *5*, Q01004. https://doi.org/10.1029/2003GC000604

Benz, H. M., Chouet, B. A., Dawson, P. B., Lahr, J. C., Page, R. A., & Hole, J. A. (1996). Three-dimensional P and S wave velocity structure of Redoubt Volcano, Alaska. *Journal of Geophysical Research*, *101*(B4), 8111–8128. https://doi.org/10.1029/95JB03046

Bratt, S. R., & Solomon, S. C. (1984). Compressional and shear wave structure of the East Pacific Rise at 11°20′N: Constraints from three-component ocean bottom seismometer data. *Journal of Geophysical Research*, *89*(B7), 6095–6110. https://doi.org/10.1029/JB089iB07p06095

Buck, W. R., Carbotte, S. M., & Mutter, C. (1997). Controls on extrusion at mid-ocean ridges. *Geology*, *25*(10), 935. https://doi.org/10.1130/0091-7613(1997)025<0935:COEAMO>2.3.CO;2

Butterfield, D. A., Massoth, G. J., McDuff, R. E., Lupton, J. E., & Lilley, M. D. (1990). Geochemistry of hydrothermal fluids from Axial Seamount hydrothermal emissions study vent field, Juan de Fuca Ridge: Subseafloor boiling and subsequent fluid-rock interaction. *Journal of Geophysical Research*, *95*(B8), 12895. https://doi.org/10.1029/JB095iB08p12895

Canales, J. P., Singh, S. C., Detrick, R. S., Carbotte, S. M., Harding, A., Kent, G. M., et al. (2006). Seismic evidence for variations in axial magma chamber properties along the southern Juan de Fuca Ridge. *Earth and Planetary Science Letters*, *246*(3–4), 353–366. https://doi.org/10.1016/J.EPSL.2006.04.032

Carbotte, S. M., Detrick, R. S., Harding, A., Canales, J. P., Babcock, J., Kent, G., et al. (2006). Rift topography linked to magmatism at the intermediate spreading Juan de Fuca Ridge. *Geology*, *34*(3), 209. https://doi.org/10.1130/G21969.1

Carbotte, S. M., Marjanović, M., Carton, H., Mutter, J. C., Canales, J. P., Nedimović, M. R., et al. (2013). Fine-scale segmentation of the crustal magma reservoir beneath the East Pacific Rise. *Nature Geoscience*, *6*(10), 866–870. https://doi.org/10.1038/ngeo1933

Carbotte, S. M., Mutter, C., Mutter, J., & Ponce-Correa, G. (1998). Influence of magma supply and spreading rate on crustal magma bodies and emplacement of the extrusive layer: Insights from the East Pacific Rise at lat 16°N. *Geology*, *26*(5), 455–458. https://doi.org/10.1130/0091-7613(1998)026<0455:IOMSAS>2.3.CO;2

Carbotte, S. M., Nedimović, M. R., Canales, J. P., Kent, G. M., Harding, A. J., & Marjanović, M. (2008). Variable crustal structure along the Juan de Fuca Ridge: Influence of on-axis hot spots and absolute plate motions. *Geochemistry, Geophysics, Geosystems*, *9*, Q08001. https://doi.org/10.1029/2007GC001922

Caress, D. W., Clague, D. A., Paduan, J. B., Martin, J. F., Dreyer, B. M., Chadwick, W. W., et al. (2012). Repeat bathymetric surveys at 1-metre resolution of lava flows erupted at Axial Seamount in April 2011. *Nature Geoscience*, *5*(7), 483–488. https://doi.org/10.1038/ngeo1496

Carlson, R. L. (2014). The influence of porosity and crack morphology on seismic velocity and permeability in the upper oceanic crust. *Geochemistry, Geophysics, Geosystems*, *15*, 10–27. https://doi.org/10.1002/2013GC004965

Chadwick, W. W., Clague, D. A., Embley, R. W., Perfit, M. R., Butterfield, D. A., Caress, D. W., et al. (2013). The 1998 eruption of Axial Seamount: New insights on submarine lava flow emplacement from high-resolution mapping. *Geochemistry, Geophysics, Geosystems*, *14*, 3939–3968. https://doi.org/10.1002/ggge.20202

Chadwick, W. W., Nooner, S. L., Butterfield, D. A., & Lilley, M. D. (2012). Seafloor deformation and forecasts of the April 2011 eruption at Axial Seamount. *Nature Geoscience*, *5*(7), 474–477. https://doi.org/10.1038/ngeo1464

Chadwick, W. W., Paduan, J. B., Clague, D. A., Dreyer, B. M., Merle, S. G., Bobbitt, A. M., et al. (2016). Voluminous eruption from a zoned magma body after an increase in supply rate at Axial Seamount. *Geophysical Research Letters*, *43*, 12,12–63,70. https://doi.org/10.1002/2016GL071327

Chen, Y. J., & Lin, J. (2004). High sensitivity of ocean ridge thermal structure to changes in magma supply: The Galápagos Spreading Center. *Earth and Planetary Science Letters*, *221*(1–4), 263–273. https://doi.org/10.1016/S0012-821X(04)00099-8

Chen, Y. J., & Morgan, J. P. (1996). The effects of spreading rate, the magma budget, and the geometry of magma emplacement on the axial heat flux at mid-ocean ridges. *Journal of Geophysical Research*, *101*(B5), 11,475–11,482. https://doi.org/10.1029/96JB00330

Christeson, G. L., Karson, J. A., & McIntosh, K. D. (2010). Mapping of seismic layer 2A/2B boundary above the sheeted dike unit at intermediate spreading crust exposed near the Blanco Transform. *Geochemistry, Geophysics, Geosystems*, *11*, Q03015. https://doi.org/10.1029/2009GC002864

Christeson, G. L., McIntosh, K. D., & Karson, J. A. (2007). Inconsistent correlation of seismic layer 2a and lava layer thickness in oceanic crust. *Nature*, *445*(7126), 418–421. https://doi.org/10.1038/nature05517

Christeson, G. L., Purdy, G. M., & Fryer, G. J. (1994). Seismic constraints on shallow crustal emplacement processes at the fast spreading East Pacific Rise. *Journal of Geophysical Research*, *99*(B9), 17,917-957,973. Retrieved from file:///Users/michw/Library/Application Support/Mendeley Desktop/Downloaded/Christeson, Purdy, Fryer - 1994 - Seismic constraints on shallow crustal emplacement processes at the fast spreading East Pacific Rise.pdf

Christeson, G. L., Shaw, P. R., & Garmany, J. D. (1997). Shear and compressional wave structure of the East Pacific Rise, 9°-10°N. *Journal of Geophysical Research*, *102*(B4), 7821–7835. https://doi.org/10.1029/96JB03901

Clague, D. D. A., Paduan, J. J. B., Caress, D. D. W., Chadwick, W. W. Jr., Le Saout, M., Dreyer, B. M. B., & Portner, R. A. (2017). High-Resolution AUV mapping and targeted ROV observations of three historic lava flows at Axial Seamount. *Oceanography*, *30*(4), 82–99. https://doi.org/https://doi.org/10.5670/oceanog.2017.426

Collier, J. S., & Singh, S. C. (1998). Poisson's ratio structure of young oceanic crust. *Journal of Geophysical Research*, *103*(B9), 20,981–20,996. https://doi.org/10.1029/98JB01980

Combier, V., Seher, T., Singh, S. C., Crawford, W. C., Cannat, M., Escartín, J., & Dusunur, D. (2015). Three-dimensional geometry of axial magma chamber roof and faults at Lucky Strike volcano on the Mid-Atlantic Ridge. *Journal of Geophysical Research: Solid Earth*, *120*, 5379–5400. https://doi.org/10.1002/2015JB012365

Crawford, W. C., Rai, A., Singh, S. C., Cannat, M., Escartin, J., Wang, H., et al. (2013). Hydrothermal seismicity beneath the summit of Lucky Strike volcano, Mid-Atlantic Ridge. *Earth and Planetary Science Letters*, *373*, 118–128. https://doi.org/10.1016/j.epsl.2013.04.028

Crisp, J. A. (1984). Rates of magma emplacement and volcanic output. *Journal of Volcanology and Geothermal Research*, *20*(3–4), 177–211. https://doi.org/10.1016/0377-0273(84)90039-8

Detrick, R. S., Buhl, P., Vera, E., Mutter, J., Orcutt, J., Madsen, J., & Brocher, T. (1987). Multi-channel seismic imaging of a crustal magma chamber along the East Pacific Rise. *Nature*, *326*(6108), 35–41. https://doi.org/10.1038/326035a0

Detrick, R. S., Harding, A. J., Kent, G. M., Orcutt, J. A., Mutter, J. C., & Buhl, P. (1993). Seismic Structure of the Southern East Pacific Rise. *Science*, *259*(5094), 499–503. https://doi.org/10.1126/science.259.5094.499

Dunn, R. A., Toomey, D. R., & Solomon, S. C. (2000). Three-dimensional seismic structure and physical properties of the crust and shallow mantle beneath the East Pacific Rise at 9°30'N. *Journal of Geophysical Research*, *105*(B10), 23,537–23,555. https://doi.org/10.1029/2000JB900210

Dziak, R. P., & Fox, C. G. (1999). The January 1998 Earthquake swarm at Axial Volcano, Juan de Fuca Ridge: Hydroacoustic evidence of seafloor volcanic activity. *Geophysical Research Letters*, *26*(23), 3429–3432. https://doi.org/10.1029/1999GL002332

Dziak, R. P., Haxel, J. H., Bohnenstiehl, D. R., Chadwick, W. W., Nooner, S. L., Fowler, M. J., et al. (2012). Seismic precursors and magma ascent before the April 2011 eruption at Axial Seamount. *Nature Geoscience*, *5*(7), 478–482. https://doi.org/10.1038/ngeo1490

Folch, A., & Martí, J. (2004). Geometrical and mechanical constraints on the formation of ring-fault calderas. *Earth and Planetary Science Letters*. https://doi.org/10.1016/S0012-821X(04)00101-3

Fowler, C. M. R. (1976). Crustal structure of the Mid-Atlantic ridge crest at 37 N. *Geophysical Journal International*, *47*(3), 459–491. https://doi.org/10.1111/j.1365-246X.1976.tb07097.x

Fox, C. G. (1999). In situ ground deformation measurements from the summit of Axial Volcano during the 1998 volcanic episode. *Geophysical Research Letters*, *26*(23), 3437–3440. https://doi.org/10.1029/1999GL900491

German, C. R., Lin, J., & Parson, L. M. (2004). In C. R. German, J. Lin, & L. M. Parson (Eds.), *Mid-Ocean Ridges: Hydrothermal interactions between the lithosphere and oceans*, (Vol. 148). Washington, D. C: American Geophysical Union. https://doi.org/10.1002/9781118665879

Geyer, A., Folch, A., & Martí, J. (2006). Relationship between caldera collapse and magma chamber withdrawal: An experimental approach. *Journal of Volcanology and Geothermal Research*. https://doi.org/10.1016/j.jvolgeores.2006.05.001

Golden, C. E., Webb, S. C., & Sohn, R. A. (2003). Hydrothermal microearthquake swarms beneath active vents at Middle Valley, northern Juan de Fuca Ridge. *Journal of Geophysical Research*, *108*(B1), 2027. https://doi.org/10.1029/2001JB000226

Gomberg, J. (1990). The effect of S-wave arrival times on the accuracy of hypocenter estimation. *Bulletin of the Seismological Society of America*, *80*(6), 1605–1628.

Gudmundsson, A., Fjeldskaar, I., & Brenner, S. L. (2002). Propagation pathways and fluid transport of hydrofractures in jointed and layered rocks in geothermal fields. *Journal of Volcanology and Geothermal Research*, *116*(3–4), 257–278. https://doi.org/10.1016/S0377-0273(02)00225-1

Hammond, S. R., Empley, R. W., & Baker, E. T. (2015). The NOAA vents program 1983 to 2013 thirty years of ocean exploration and research. *Oceanography*, *28*(1), 160–173. https://doi.org/10.1017/CBO9781107415324.004

Hardebeck, J. L., Survey, U. S. G., & Park, M. (2008). HASH A FORTRAN Program for Computing Earthquake First- Motion Focal Mechanisms – v1. 2 – January 31, 2008.

Harding, A. J., Kent, G. M., Blackman, D. K., Singh, S., & Canales, J. P. (2007). A New Method for MCS refraction data analysis of the uppermost section at a Mid-Atlantic Ridge core complex. American Geophysical Union, Fall Meeting 2007, Abstract Id. S13A-03. Retrieved from. http://adsabs.harvard.edu/abs/2007AGUFM.S13A..03H

Harding, A. J., Kent, G. M., & Orcutt, J. A. (1993). A multichannel seismic investigation of upper crustal structure at 9°N on the East Pacific Rise: Implications for crustal accretion. *Journal of Geophysical Research*, *98*(B8), 13,925–13,944. https://doi.org/10.1029/93JB00886

Husen, S., Smith, R. B., & Waite, G. P. (2004). Evidence for gas and magmatic sources beneath the Yellowstone volcanic field from seismic tomographic imaging. *Journal of Volcanology and Geothermal Research*, *131*(3–4), 397–410. https://doi.org/10.1016/S0377-0273(03)00416-5

Hyndman, R. D. (1979). Poisson's ratio in the oceanic crust—A review. *TectonoPhysics*, *59*(1–4), 321–333. https://doi.org/10.1016/0040-1951(79)90053-2

Jaxybulatov, K., Koulakov, I., Seht, M. I., Klinge, K., Reichert, C., Dahren, B., & Troll, V. R. (2011). Evidence for high fluid/melt content beneath Krakatau volcano (Indonesia) from local earthquake tomography. *Journal of Volcanology and Geothermal Research*, *206*(3–4), 96–105. https://doi.org/10.1016/j.jvolgeores.2011.06.009

Johnson, H. P., & Embley, R. W. (1990). Axial seamount: An active ridge axis volcano on the Central Juan De Fuca Ridge. *Journal of Geophysical Research*, *95*(B8), 12689. https://doi.org/10.1029/JB095iB08p12689

Kelley, D. S., Delaney, J. R., & Juniper, S. K. (2014). Establishing a new era of submarine volcanic observatories: Cabling Axial Seamount and the Endeavour Segment of the Juan de Fuca Ridge. *Marine Geology*. https://doi.org/10.1016/j.margeo.2014.03.010

Kim, E., Toomey, D. R., Hooft, E. E. E., Wilcock, W. S. D., Weekly, R. T., Lee, S., & Kim, Y. H. (2018). Upper crustal Vp/Vs ratios at the Endeavour segment, Juan de Fuca Ridge, from joint inversion of P and S travel times: Implications for hydrothermal circulation. *Geochemistry, Geophysics, Geosystems*, *20*, 208–229. https://doi.org/10.1029/2018GC007921

Klein, F. W. (2002). User's guide to HYPOINVERSE-2000, a Fortran program to solve for earthquake locations and magnitudes. *Open-File Report*. https://doi.org/10.3133/OFR02171

Kong, L. S. L. (1990). *Variations in structure and tectonics along the Mid-Atlantic Ridge, 23 degress N and 26 degrees N*. Woods Hole, MA: Massachusetts Institute of Technology and Woods Hole Oceanographic Institution. https://doi.org/10.1575/1912/5421

Koulakov, I. (2009). LOTOS code for local earthquake tomographic inversion: Benchmarks for testing tomographic algorithms. *Bulletin of the Seismological Society of America*, *99*(1), 194–214. https://doi.org/10.1785/0120080013

Koulakov, I., Gordeev, E. I., Dobretsov, N. L., Vernikovsky, V. A., Senyukov, S., & Jakovlev, A. (2011). Feeding volcanoes of the Kluchevskoy group from the results of local earthquake tomography. *Geophysical Research Letters*, *38*, L09305. https://doi.org/10.1029/2011GL046957

Koulakov, I., Yudistira, T., & Luehr, B.-G. (2009). Toba caldera complex (Northern Sumatra) from local earthquake tomography. *Geophysical Journal International*, *177*, 1121–1139. https://doi.org/10.1111/j.1365-246X.2009.04114.x

Lee, W. H., & Lahr, J. C. (1975). HYPO71 (revised; a computer program for determining hypocenter, magnitude, and first motion pattern of local earthquakes). *Open-File Report*. https://doi.org/10.3133/OFR75311

Lees, J. M. (2007). Seismic tomography of magmatic systems. *Journal of Volcanology and Geothermal Research*, *167*(1–4), 37–56. https://doi.org/10.1016/J.JVOLGEORES.2007.06.008

Levy, S., Bohnenstiehl, D. R., Sprinkle, P., Boettcher, M. S., Wilcock, W. S. D., Tolstoy, M., & Waldhauser, F. (2018). Mechanics of fault reactivation before, during, and after the 2015 eruption of Axial Seamount. *Geology*, 3–6. https://doi.org/10.1130/G39978.1

Lomax, A., Virieux, J., Volant, P., & Berge-Thierry, C. (2000). Probabilistic Earthquake Location in 3D and Layered Models. In C. H. Thurber, & N. Rabinowitz (Eds.), *Advances in Seismic Event Location. Modern Approaches in Geophysics* (Vol. 18, pp. 101–134). Dordrecht: Springer. https://doi.org/10.1007/978-94-015-9536-0_5

Ludwig, R. J., Iturrino, G. J., & Rona, P. A. (1998). Seismic velocity-porosity relationship of sulfide, sulfate, and basalt samples from the TAG hydrothermal mound. In *Proceedings of the Ocean Drilling Program, 158 Scientific Results* (Vol. 158, Chap. 23, pp. 313–327). College Station, TX: Ocean Drilling Program. https://doi.org/10.2973/odp.proc.sr.158.225.1998

Magde, L. S., Barclay, A. H., Toomey, D. R., Detrick, R. S., & Collins, J. A. (2000). Crustal magma plumbing within a segment of the Mid-Atlantic Ridge, 35°N. *Earth and Planetary Science Letters*, *175*(1–2), 55–67. https://doi.org/10.1016/S0012-821X(99)00281-2

Molina, I., Kumagai, H., Le Pennec, J.-L., & Hall, M. (2005). Three-dimensional P-wave velocity structure of Tungurahua Volcano, Ecuador. *Journal of Volcanology and Geothermal Research*, *147*(1–2), 144–156. https://doi.org/10.1016/J.JVOLGEORES.2005.03.011

Moser, T. J. (1991). Shortest path calculation of seismic rays. *Geophysics*, *56*(1), 59–67. https://doi.org/10.1190/1.1442958

Nooner, S. L., & Chadwick, W. W. (2016). Inflation-predictable behavior and co-eruption deformation at Axial Seamount. *Science (New York, N.Y.)*, *354*(6318), 1399–1403. https://doi.org/10.1126/science.aah4666

Paige, C., & Saunders, M. (1982). LSQR: An algorithm for sparse linear equations and sparse least squares. *ACM Transactions on Mathematical Software*, *8*(1), 43–71.

Parnell-Turner, R., Sohn, R. A., Peirce, C., Reston, T. J., MacLeod, C. J., Searle, R. C., & Simão, N. M. (2017). Oceanic detachment faults generate compression in extension. *Geology*, *45*(10), 923–926. https://doi.org/10.1130/G39232.1

Pavlis, G. L., & Booker, J. R. (1980). The mixed discrete-continuous inverse problem: Application to the simultaneous determination of earthquake hypocenters and velocity structure. *Journal of Geophysical Research*, *85*(B9), 4801. https://doi.org/10.1029/JB085iB09p04801

Podvin, P., & Lecomte, I. (1991). Finite-difference computation of traveltimes in very contrasted velocity models—A massively parallel approach and its related tools. *Geophysical Journal International*, *105*(1), 271–284. https://doi.org/10.1111/j.1365-246X.1991.tb03461.x

Pontbriand, C. W., & Sohn, R. A. (2014). Microearthquake evidence for reaction-driven cracking within the Trans-Atlantic Geotraverse active hydrothermal deposit. *Journal of Geophysical Research: Solid Earth*, *119*, 822–839. https://doi.org/10.1002/2013JB010110

Prôno, E., Battaglia, J., Monteiller, V., Got, J.-L., & Ferrazzini, V. (2009). P-wave velocity structure of Piton de la Fournaise volcano deduced from seismic data recorded between 1996 and 1999. *Journal of Volcanology and Geothermal Research*, *184*(1–2), 49–62. https://doi.org/10.1016/J.JVOLGEORES.2008.12.009

Sanders, C. O., Ponko, S. C., Nixon, L. D., & Schwartz, E. A. (1995). Seismological evidence for magmatic and hydrothermal structure in Long Valley caldera from local earthquake attenuation and velocity tomography. *Journal of Geophysical Research*, *100*(B5), 8311–8326. https://doi.org/10.1029/95JB00152

Shearer, P. M. (1988). Cracked media, Poisson's ratio and the structure of the upper oceanic crust. *Geophysical Journal International*, *92*(2), 357–362. https://doi.org/10.1111/j.1365-246X.1988.tb01149.x

Singh, S. C., Kent, G. M., Collier, J. S., Harding, A. J., & Orcutt, J. A. (1998). Melt to mush variations in crustal magma properties along the ridge crest at the southern East Pacific Rise. *Nature*, *394*(6696), 874–878. https://doi.org/10.1038/29740

Sinton, J. M., & Detrick, R. S. (1992). Mid-ocean ridge magma chambers. *Journal of Geophysical Research*, *97*(B1), 197. https://doi.org/10.1029/91JB02508

Sluis, A., & Vorst, H. A. (1987). Numerical solution of large, sparse linear algebraic systems arising from tomographic problems. In *Seismic Tomography*, (pp. 49–83). Dordrecht: Springer Netherlands. https://doi.org/10.1007/978-94-009-3899-1_3

Sohn, R. A., Barclay, A. H., & Webb, S. C. (2004). Microearthquake patterns following the 1998 eruption of Axial Volcano, Juan de Fuca Ridge: Mechanical relaxation and thermal strain. *Journal of Geophysical Research*, *109*, B01101. https://doi.org/10.1029/2003JB002499

Sohn, R. A., Hildebrand, J. A., & Webb, S. C. (1998). Postrifting seismicity and a model for the 1993 diking event on the Coaxial segment, Juan de Fuca Ridge. *Journal of Geophysical Research*, *103*(B5), 9867–9877. https://doi.org/10.1029/98JB00391

Sohn, R. A., Hildebrand, J. A., & Webb, S. C. (1999). A microearthquake survey of the high-temperature vent fields on the volcanically active East Pacific Rise (9°50′N). *Journal of Geophysical Research*, *104*(B11), 25,367–25,377. https://doi.org/10.1029/1999JB900263

Spudich, P., & Orcutt, J. (1980). A new look at the seismic velocity structure of the oceanic crust. *Reviews of Geophysics*, *18*(3), 627. https://doi.org/10.1029/RG018i003p00627

Tan, Y. J., Tolstoy, M., Waldhauser, F., & Wilcock, W. S. D. (2016). Dynamics of a seafloor-spreading episode at the East Pacific Rise. *Nature*, *540*(7632), 261–265. https://doi.org/10.1038/nature20116

Toksöz, M. N. (1976). Velocities of seismic waves in porous rocks. *Geophysics*, *41*(4), 621. https://doi.org/10.1190/1.1440639

Tolstoy, M., Cowen, J. P., Baker, E. T., Fornari, D. J., Rubin, K. H., Shank, T. M., et al. (2006). A sea-floor spreading event captured by seismometers. *Science (New York, N.Y.)*, *314*(5807), 1920–1922. https://doi.org/10.1126/science.1133950

Tolstoy, M., Waldhauser, F., Bohnenstiehl, D. R., Weekly, R. T., & Kim, W.-Y. (2008). Seismic identification of along-axis hydrothermal flow on the East Pacific Rise. *Nature*, *451*(7175), 181–184. https://doi.org/10.1038/nature06424

Toomey, D. R., Jousselin, D., Dunn, R. A., Wilcock, W. S. D., & Detrick, R. S. (2007). Skew of mantle upwelling beneath the East Pacific Rise governs segmentation. *Nature*, *446*(7134), 409–414. https://doi.org/10.1038/nature05679

Toomey, D. R., Solomon, S. C., & Purdy, G. M. (1988). Microearthquakes beneath Median Valley of Mid-Atlantic Ridge near 23°N: Tomography and tectonics. *Journal of Geophysical Research*, *93*(B8), 9093. https://doi.org/10.1029/JB093iB08p09093

Toomey, D. R., Solomon, S. C., Purdy, G. M., & Murray, M. H. (1985). Microearthquakes beneath the Median Valley of the Mid-Atlantic Ridge near 23°N: Hypocenters and focal mechanisms. *Journal of Geophysical Research*, *90*(B7), 5443–5458. https://doi.org/10.1029/JB090iB07p05443

Um, J., & Thurber, C. (1987). FAST ALGORITHM FOR TWO-POINT SEISMIC RAY TRACING. *Bulletin of the Seismological Society of America*. https://doi.org/10.1130/0-8137-2302-7.347

Vanorio, T., Virieux, J., Capuano, P., & Russo, G. (2005). Three-dimensional seismic tomography from P wave and S wave microearthquake travel times and rock physics characterization of the Campi Flegrei Caldera. *Journal of Geophysical Research*, *110*, B03201. https://doi.org/10.1029/2004JB003102

Vera, E. E., Mutter, J. C., Buhl, P., Orcutt, J. A., Harding, A. J., Kappus, M. E., et al. (1990). The structure of 0- to 0.2-m.y.-old oceanic crust at 9°N on the East Pacific Rise from expanded spread profiles. *Journal of Geophysical Research*, *95*(B10), 15529. https://doi.org/10.1029/JB095iB10p15529

Waldhauser, F., & Ellsworth, W. L. (2000). A double-difference earthquake location algorithm: Method and application to the Northern Hayward Fault, California. *Bulletin of the Seismological Society of America*, *90*(6), 1353–1368. https://doi.org/10.1785/0120000006

West, M., Menke, W., Tolstoy, M., Webb, S., & Sohn, R. (2001). Magma storage beneath Axial Volcano on the Juan de Fuca mid-ocean ridge. *Nature*, *413*(6858), 833–836. https://doi.org/10.1038/35101581

Wilcock, W. S. D., Archer, S. D., & Purdy, G. M. (2002). Microearthquakes on the Endeavour segment of the Juan de Fuca Ridge. *Journal of Geophysical Research*, *107*(B12), 2336. https://doi.org/10.1029/2001JB000505

Wilcock, W. S. D., Dziak, R., Tolstoy, M., Chadwick, W., Nooner, S., Bohnenstiel, D., et al. (2018). The recent volcanic history of Axial Seamount: Geophysical insights into past eruption dynamics with an eye toward enhanced observations of future eruptions. *Oceanography*, *31*(1), 114–123. https://doi.org/10.5670/oceanog.2018.117

Wilcock, W. S. D., Hooft, E. E. E., Toomey, D. R., McGill, P. R., Barclay, A. H., Stakes, D. S., & Ramirez, T. M. (2009). The role of magma injection in localizing black-smoker activity. *Nature Geoscience*, *2*(7), 509–513. https://doi.org/10.1038/ngeo550

Wilcock, W. S. D., Tolstoy, M., Waldhauser, F., Garcia, C., Tan, Y. J., Bohnenstiehl, D. R., et al. (2016). Seismic constraints on caldera dynamics from the 2015 Axial Seamount eruption. *Science*, *354*(6318), 1395–1399. https://doi.org/10.1126/science.aah5563

Wilcock, W. S. D., Waldhauser, F., & Tolstoy, M. (2017). Catalogs of earthquake recorded on Axial Seamount from January, 2015 through November, 2015 (investigators William Wilcock, Maya Tolstoy, Felix Waldhauser). *Interdisciplinary Earth Data Alliance*. https://doi.org/10.1594/IEDA/323843

Xu, M., Pablo Canales, J., Carbotte, S. M., Carton, H., Nedimović, M. R., & Mutter, J. C. (2014). Variations in axial magma lens properties along the East Pacific Rise (9°30′N-10°00′N) from swath 3-D seismic imaging and 1-D waveform inversion. *Journal of Geophysical Research: Solid Earth*, *119*, 2721–2744. https://doi.org/10.1002/2013JB010730

Zandomeneghi, D., Barclay, A., Almendros, J., Godoy, J. M. I., Wilcock, W. S. D., & Ben-Zvi, T. (2009). Crustal structure of Deception Island volcano from P wave seismic tomography: Tectonic and volcanic implications. *Journal of Geophysical Research*, *114*, B06310. https://doi.org/10.1029/2008JB006119

Zollo, A., Judenherc, S., Auger, E., D'Auria, L., Virieux, J., Capuano, P., et al. (2003). Evidence for the buried rim of Campi Flegrei caldera from 3-d active seismic imaging. *Geophysical Research Letters*, *30*(19), 2002. https://doi.org/10.1029/2003GL018173